

Energy Relaxation of N₂O in Gaseous, Supercritical and Liquid Xenon and SF₆

Kai Töpfer,[†] Shyamsunder Erramilli,[‡] Lawrence D. Ziegler,[¶] and Markus
Meuwly^{*,†,§}

[†]*Department of Chemistry, University of Basel, Klingelbergstrasse 80, CH-4056 Basel,
Switzerland*

[‡]*Department of Physics and the Photonics Center, Boston University, 590 Commonwealth
Ave, MA 02215, Boston*

[¶]*Department of Chemistry and the Photonics Center, Boston University, 8 St Mary's St,
MA 02215, Boston*

[§]*Department of Chemistry, Brown University, Providence, RI 02912, USA*

E-mail: m.meuwly@unibas.ch

Abstract

Rotational and vibrational energy relaxation (RER and VER) of N₂O embedded in xenon and SF₆ environments ranging from the gas phase to the liquid, including the supercritical regime, is studied at a molecular level. Calibrated intermolecular interactions from high-level electronic structure calculations, validated against experiments for the pure solvents were used to carry out classical molecular dynamics simulations corresponding to experimental state points for near-critical isotherms. Computed RER rates in low-density solvent of $k_{\text{rot}}^{\text{Xe}} = (3.67 \pm 0.25) \cdot 10^{10} \text{ s}^{-1}\text{M}^{-1}$ and $k_{\text{rot}}^{\text{SF}_6} = (1.25 \pm 0.12) \cdot 10^{11} \text{ s}^{-1}\text{M}^{-1}$ compare well with rates determined by analysis of 2-dimensional infrared experiments. Simulations find that an isolated binary collision (IBC) description is successful up to solvent concentrations of $\sim 4 \text{ M}$. For higher densities, including the supercritical regime, the simulations do not correctly describe RER, probably due to neglect of solvent-solute coupling in the analysis of the rotational motion. For VER, the near-quantitative agreement between simulations and pump-probe experiments captures the solvent density-dependent trends.

Introduction

Understanding the precise molecular level details of rotational and vibrational energy relaxation dynamics in high density gas and supercritical fluid (SCF) solutions is of fundamental importance for the description, optimization and control of chemical reactivity in inherently dense media. For example, dense fluids at high temperatures and pressures, often in supercritical (sc) regimes, are solvent environments where many combustion reactions occur.¹⁻³ Furthermore, SCFs offer the possibility for selective control of chemical processes including energy relaxation/transfer dynamics, and have already been successfully employed in a range of applications.⁴⁻¹⁰ Aside from offering the “green” potential to replace organic solvents (e.g. scH₂O or scCO₂), local density augmentation and the dynamics associated with the

long-spatial correlations that develop in near critical state points contribute to the special solvation properties of near critical fluids.^{4,11,12} These density correlation length increases result in a corresponding correlation relaxation time increase at the critical point, often described as critical slowing and evident in scattering experiments¹³⁻¹⁵ and simulations.^{16,17}

In prior ultrafast studies of dense gas and supercritical fluid solutions, two-dimensional infrared (2DIR) experiments have revealed rates of rotational energy relaxation (RER) as a function of solvent density for the N₂O asymmetric stretching mode (ν_{as}) in SF₆ and Xe even in the absence of any rotational features in the corresponding ν_{as} rovibrational spectrum.¹⁸⁻²⁰ Pump-probe measurements provide vibrational energy relaxation (VER) rates for these same high density state points. A simple isolated binary collision (IBC) model was sufficient to describe RER of N₂O ν_{as} up to SF₆ and Xe solvent densities of ≈ 4 M for $T \leq 1.01T_c$ isotherms derived from 2DIR measurements.²⁰ However, the RER dynamics of N₂O in these two similar non-dipolar solvents show different concentration dependencies as the critical density is approached and where many body effects begin to play a larger role for solvation.²⁰ The RER of N₂O is slower than the IBC predicted rates in the density region (≈ 4 M - ≈ 6 M) of the SF₆ critical point ($\rho_c(\text{SF}_6) = 5.09$ M) and attributed to the longer length scale, slower density fluctuations coupling to the closest N₂O solvation shells. However, no such slowing effect was observed for N₂O RER in xenon. For xenon densities $> \sim 4$ M, the RER rate monotonically increased through the critical point region ($\rho_c(\text{Xe}) = 8.40$ M). It was hypothesized that the many body interactions at the higher critical density for the xenon solvent shielded the N₂O rotors from coupling to the long correlation length fluctuations. N₂O rotational relaxation in both solvents is a highly efficient process. Following ν_{as} excitation rotational equilibrium is re-established after 1.7 and 2.4 collisions in SF₆ and Xe respectively in the IBC density region.²⁰

Rotational and vibrational equilibrium are established on very different timescales following

N_2O ν_{as} excitation in these high density gas and SCF SF_6 and Xe solvents.²⁰ While only a couple of collisions are required for N_2O rotations to thermalize in both solvents, the VER of N_2O may take hundreds of collisions or more to return the molecule fully to thermal equilibrium. The density dependence of N_2O VER is also strikingly different in xenon and SF_6 , and underscores that VER has a highly variable rate due to the inherently quantum nature ($\hbar\omega_{\text{vib}} = kT$) of this relaxation mechanism. The N_2O ν_{as} lifetime is ≈ 300 times shorter in SF_6 than in xenon than because xenon has no possible resonant $\text{V} \rightarrow \text{V}$, solute \rightarrow solvent, energy transfer relaxation pathway as found for relatively efficient VER from N_2O ν_{as} in SF_6 . The first step in N_2O ν_{as} VER in SF_6 is the collision enabled intramolecular relaxation to the N_2O symmetric stretching mode before a much slower return to the ground vibrational state. Furthermore, VER is nearly an order of magnitude slower for this initial VER component in SF_6 as compared to RER, and a critical slowing effect is not as clearly evident.²⁰ The density dependence of the N_2O ν_{as} rovibrational absorption line shapes in SF_6 and xenon were well-captured in a previous classical MD simulation study.²¹ Even the rovibrational spectral contours, inherently determined by J,M quantum transition selection rules, were accurately duplicated by these classical simulation results. The goal of this current report is to test the ability of this same simulation approach to capture the previously reported N_2O ν_{as} rotational and vibrational relaxation dynamics determined by these 2DIR and pump-probe measurements spanning the dense gas to supercritical density regime in SF_6 and Xe.

Relaxation phenomena in liquids provide valuable information about intermolecular interactions and coupling between solvent and solute modes. In the present work RER and VER of N_2O as the solute immersed in Xe and SF_6 as atomic and molecular solvents at a wide range of densities is investigated from atomistic simulations. The environments are under conditions which range from gaseous to the supercritical and regular liquids.

The present work is structured as follows. First, the methods are presented, followed by the

validation of the intermolecular interactions. Next, results on the RER and VER of N₂O are presented and discussed. Finally, conclusions are drawn.

Methods

Inter- and Intramolecular Interactions

The N₂O PES: The intramolecular potential energy surface (PES) of N₂O in its electronic ground state (¹A') is provided by a machine-learned representation using the reproducing kernel Hilbert space (RKHS) method.^{22,23} Reference energies at the CCSD(T)-F12/aug-cc-pVQZ level of theory were determined on a grid of Jacobi coordinates (R, r, θ) with r the N-N separation, R the distance between the center of mass of the diatom and the oxygen atom, and θ the angle between the two distance vectors. All calculations were carried out using the MOLPRO package.²⁴ The full-dimensional RKHS model for a N₂O potential energy surface was originally developed for the investigation of N+NO collision reaction dynamics.²³ The Pearson coefficient R^2 of the RKHS representation and the full set of reference values is 0.99983 and the root mean squared error (RMSE) between RKHS and reference energies up to 20 kcal/mol above the equilibrium structure (78 reference energies) is 0.13 kcal/mol.

The Solvent PES: Intra- and intermolecular force field parameters for SF₆ were those from the work of Samios *et al.*²⁵ Intermolecular interactions were based on Lennard-Jones potentials only and the parameters were optimized such that MD simulations of pure SF₆ reproduce the experimentally observed pVT state points for liquid and gas SF₆, as well as the states of liquid-vapor coexistence below and supercritical fluid above the critical temperature $T_c(\text{SF}_6) = 318.76$ K, respectively.^{26,27} For Xe the Lennard-Jones parameters were optimized to reproduce the pVT state points of gaseous, supercritical and liquid Xe at different densities and temperatures below and above the critical temperature of $T_c(\text{Xe}) = 289.74$ K.^{26,27}

The Xe–Xe Lennard-Jones (LJ) potential parameters for the van-der-Waals (vdW) potential energy contribution were fit to match experimental pVT state points of xenon, which were computed with a similar setup as used by Samios *et al.* to fit the force field parameters for SF₆.²⁵ A set of $N_{pVT} = 44$ experimentally measured pVT state points of xenon at temperatures (number of state points) 273.15 (5), 286.65 (3), 298.15 (12), 323.15 (12) and 373.15 K (12) was selected.²⁸ For each state point a separate NVT molecular dynamics (MD) simulation was run using a Langevin thermostat with a friction coefficient of 0.1 ps⁻¹. The system contained 1200 Xe atoms, the structure was minimized, heated to the target temperature and equilibrated for a total of 100 ps with a time step of 1 fs. Next, the average pressure was determined from a 300 ps simulation and compared with the experimental reference.²⁸ The xenon LJ parameters ϵ_{Xe} and $R_{\text{min,Xe}}$ were then optimized by the Nelder–Mead method²⁹ to minimize the relative root mean square error (rRMSE) between sampled average and experimental pressures at respective volume and temperature

$$\text{rRMSE} = \sqrt{\frac{1}{N_{pVT}} \sum_i^{N_{pVT}} \left(\frac{p_{\text{sim},i}(V, T) - p_{\text{ref},i}(V, T)}{p_{\text{ref},i}(V, T)} \right)^2} \quad (1)$$

The LJ parameter set with the lowest rRMSE were chosen after the rRMSE arguably reached a convergence limit for several tens of optimization steps.

Electrostatic solvent-solute interactions were computed based on a minimally distributed charge model (MDCM) for N₂O that correctly describes higher-order multipole moments.^{30–32} For parametrization, a reference electrostatic potential (ESP) of N₂O in its linear equilibrium conformation was computed at the CCSD/aug-cc-pVTZ level using the Gaussian program package.³³ The optimized MDCM fit reproduces the ESP with a RMSE of 0.31 kcal/mol. For SF₆ in its octahedral equilibrium conformation the ESP was computed at the MP2/aug-cc-pVTZ level of theory using the Gaussian program. The RMSE between the fitted ESP from

MDCM and the reference ESP was 0.11 kcal/mol. Recently,³² non-iterative polarization was also included in MDCM, and this is also used here for N₂O, SF₆ and Xe. The polarizability of linear N₂O at the CCSD/aug-cc-pVTZ level is 2.85 Å³ (with each atom contributing ~ 0.95 Å³ per atom), compared with 2.998 Å³ from experiment.³⁴ For Xe at the CCSD/aug-cc-pVTZ the computed value of 2.96 Å³ compares with 4.005 Å³ from experiment³⁴ and for SF₆ the experimentally measured polarizability of 4.49 Å³ was used and evenly distributed over the fluorine atoms (0.74 Å³ per fluorine atom).³⁵

The LJ parameters for N₂O ($\epsilon_\alpha, R_{\min,\alpha}$ with $\alpha = \{\text{N}, \text{O}\}$) were individually optimized for each N₂O atom by least-squares fitting using the trust region reflective algorithm³⁶ to best reproduce the N₂O–Xe and N₂O–SF₆ interaction energies, respectively. Reference energies were computed for a single N₂O molecule immersed within differently dense Xe or SF₆ clusters to sample gaseous, supercritical and liquid solvent environments. For this, 50 cluster conformations for each solvent state were extracted from earlier MD simulations of difference solvent concentration.²¹ The clusters contained 3, 7, and 10 xenon atoms and 2, 6, and 10 SF₆ molecules for gaseous, supercritical and liquid samples within the radius of the first solvation shell around the N₂O center of mass of 6.5 and 7.5 Å, respectively. Cluster conformations were randomly extracted from the trajectories with the respective number of solvent atoms or molecules within the cluster radius is maintained.

Counterpoise corrected reference interaction energies between N₂O and the solvent shell of the cluster were computed at the M06-2X/aug-cc-pVTZ level of theory including D3 dispersion corrections with the Gaussian program package.^{33,37,38} Computations at the CCSD(T) level of theory, as done for the intramolecular N₂O potential, are not feasible for the interaction energies between N₂O and up to 10 Xe atoms or 10 SF₆ molecules.

Molecular Dynamics Simulations

Molecular dynamics simulations were performed with the CHARMM program package³⁹ including provisions for RKHS and MDCM.^{22,30,32} Each system (N₂O in Xe and N₂O in SF₆ at given temperature and solvent concentration) was sampled from 5 independent MD simulations with initially random solute and solvent arrangements generated using the packmol code.⁴⁰ Each simulation was initially heated and equilibrated for 100 ps each, followed by 10 ns production simulations in the *NVT* ensemble using a time step $\Delta t = 1$ fs for the leapfrog integration scheme. In total, a total of 50 ns was sampled for each system condition.

The N₂O/Xe systems were simulated at a temperature of 291.2 K and for N₂O/SF₆ the temperature was 321.9 K which both are slightly above the experimental critical temperatures for condensation of xenon and SF₆, respectively ($T_c(\text{Xe}) = 289.74$ K, $T_c(\text{SF}_6) = 318.76$ K).^{19,26,27} A Langevin thermostat (coupling 0.1 ps⁻¹) was used to maintain the temperature constant but was applied only to the solvent (Xe and SF₆) atoms. Positions and velocities of snapshots of the simulations were stored every 1 fs for analysis. As intermolecular vibrational energy transfer is slow,²⁰ the structure of N₂O was optimized and new velocities from a Boltzmann distribution at the simulation temperature were assigned to N₂O after the heating step. This ensures that the kinetic energies along the asymmetric, symmetric and bending modes match the thermal energy with respect to the target simulation temperature.

The different simulation systems were prepared according to the conditions used in the experiments.¹⁸⁻²⁰ Table S1 summarizes the N₂O concentrations $c(\text{N}_2\text{O})$, molar volumes V_m and critical density ratios $\rho^* = \rho/\rho_c$ used in the simulations. The experimentally determined critical densities are $\rho_c = 1.11$ g/ml for xenon and $\rho_c = 0.74$ g/ml for SF₆ from which critical concentrations of 8.45 M and 5.06 M for xenon and SF₆ are obtained, respectively.^{26,27} In all setups, the simulation box contained one N₂O molecule and 600 Xe atoms or 343 SF₆ molecules which corresponds to similar simulation box volumes for similar relative density

ratios of the two solvents. In the original parametrization study a simulation box containing 343 SF₆ molecules was used to fit temperature-pressure properties.²⁵

In the MD simulations for N₂O in SF₆, electrostatic and polarization interactions were only computed between the N₂O solute and SF₆ solvent. Electrostatic and polarization contributions to the SF₆ solvent-solvent interactions were neglected. Such a procedure ensures that the pure (liquid, gas) properties of the solvent are unaltered.

Analysis

Rotational Relaxation: RER times of the N₂O solute were determined by fitting single- or bi-exponential functions to the autocorrelation functions involving angular momentum-dependent quantities. The normalized correlation function $C(t)$ for a time-dependent scalar ($A(t)$) or vectorial observable ($\vec{A}(t) = \{A_x(t), A_y(t), A_z(t)\}$)

$$C(t) = \frac{\langle A(0) \cdot A(t) \rangle}{\langle A(0)^2 \rangle} \quad (2)$$

$$C(t) = \sqrt{\frac{1}{3} \sum_{i=\{x,y,z\}} \frac{\langle A_i(0) \cdot A_i(t) \rangle^2}{\langle A_i(0)^2 \rangle}} \quad (3)$$

were computed for time series of the rotational energy of N₂O where $E_{\text{rot}}(t) = |\vec{L}(t)|^2 / 2I(t)$ and $I(t)$ is the moment of inertia, the squared angular momentum $|\vec{L}(t)|^2$ and angular momentum $\vec{L}(t)$.

The amplitude A , RER rates $1/\tau_i$ and offset Δ of a single exponential function $C_1(t)$

$$C_1(t) = Ae^{-t/\tau} + \Delta \quad (4)$$

were optimized to fit the sampled rotational energy correlation function from simulations.

For the fit, the lower limit for the time was $t = 0.2$ ps, as had also been done for fitting the experimental results to avoid any pulse overlap effects,²⁰ and was restricted to $C(t) \geq 0$. It is noted that using a double exponential function does not provide improved representations of the data even near the critical point.

Vibrational Relaxation: Transition rates $k_{i \rightarrow j} = \tau_{ij}^{-1}$ for the vibrational state transition $i \rightarrow j$ of the N₂O solute in solution were computed from a Landau-Teller model^{41–45}

$$k_{i \rightarrow j} = \frac{1}{\tau_{ij}(\omega_{ij})} = \gamma_{ij} \int_{-\infty}^{\infty} dt \exp(i\omega_{ij}t) \zeta(t) \quad (5)$$

with a quantum correction factor γ_{ij} defined as

$$\gamma_{ij} = \frac{2\hbar^{-2}}{1 + \exp(-\beta\hbar\omega_{ij})}. \quad (6)$$

Here, $\zeta(t)$ is the time-dependent friction acting on the oscillation of the solute. It is derived from the correlation function

$$\zeta(t) = \langle V_{ij}(t) \cdot V_{ji}(0) \rangle \quad (7)$$

of the solute-solvent friction potential $V_{ij}(t)$.⁴² The friction potential is obtained from the solute-solvent force projection $\vec{F}_{\text{int}}(t)$ along the normal mode vector \vec{q}_i by the sum over the solute atoms α according to

$$V_{ij}(t) = \mu_i \sum_{\alpha} -\frac{1}{m_{\alpha}} \frac{\partial V_{\text{int}}(t)}{\partial \vec{q}_{i,\alpha}(t)} \cdot \vec{q}_{i,\alpha}(t) = \sum_{\alpha} \vec{F}_{\text{int},\alpha}(t) \cdot \vec{q}_{i,\alpha}(t), \quad (8)$$

where m_{α} is the atom mass of α and μ_i is the reduced mass of normal mode i .

Results

Validation of Inter- and Intramolecular Interactions

For investigating the RER and VER of N₂O in gaseous, supercritical, or liquid Xe or SF₆ environments an accurate representation of the solute-solvent interaction is crucial.¹⁸⁻²⁰ The results of the parameter optimization for the intermolecular interactions are summarized next.

Solute Potential: To establish the quality of the N₂O PES, the vibrational modes were determined by solving the 3d nuclear Schrödinger equation using the DVR3D⁴⁶ package. The computed fundamental asymmetric, symmetric, and bending vibrations were at $\nu_{as} = 2229 \text{ cm}^{-1}$, $\nu_s = 1291 \text{ cm}^{-1}$, and $\nu_b = 598 \text{ cm}^{-1}$ and agree well with 2224 cm^{-1} , 1285 cm^{-1} , and 589 cm^{-1} from experiments in the gas phase.⁴⁷⁻⁴⁹ For the bending overtone ($2\nu_b$) the computations yield 1184 cm^{-1} compared with 1168 cm^{-1} from experiments.⁴⁷⁻⁴⁹

Solvent Potential: The Xe and SF₆ solvent potential models aim at accurately reproducing the experimentally measured pVT state points. The atomic LJ parameters for SF₆ were already fitted to match reference pVT state points of pure gaseous, supercritical and liquid SF₆ systems.²⁵ In contrast, for xenon the previously used LJ parameters were fitted to match dilute gas macroscopic properties such as virial coefficient, viscosity and thermal conductivity over a wide temperature range but not specifically for correct phase transition and supercritical fluid properties.⁵⁰ As described above, the LJ parameters were refitted to reproduce the reference system pressure of pure xenon at 44 different density and temperature conditions.²⁸ Figure 1A shows the measured reference isotherms in the pVT diagram (dashed lines) and the computed pVT state points from simulations using the optimized LJ parameters with the lowest relative RMSE of 15.1% between reference and computed system pressures (absolute RMSE of 32.7 Pa). This is an improvement by a factor of ~ 5 (relative RMSE of 75.1%;

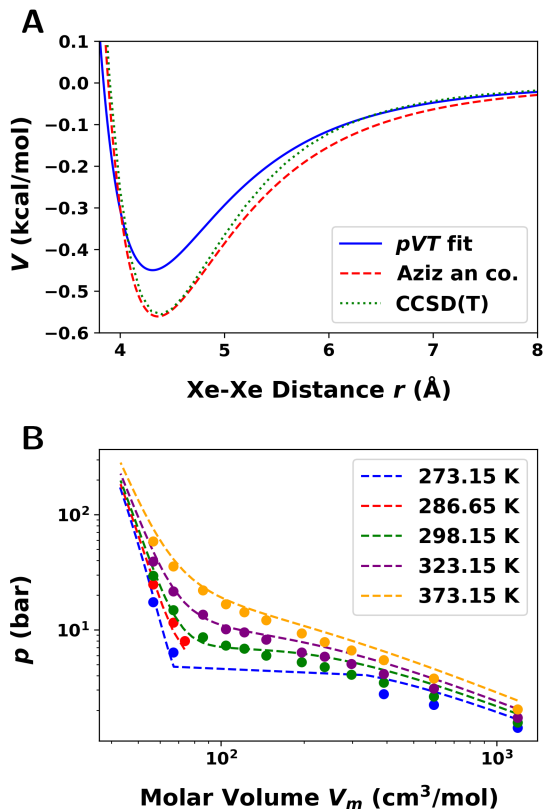


Figure 1: Panel A: Two-body interaction potential V between Xe atoms computed by Lennard-Jones potential function with the optimized LJ parameters (solid blue line) and from Aziz *et al.* (dashed red line).⁵⁰ The dotted green line shows *ab initio* reference potential for a Xe-Xe atom pair at CCSD(T)/cc-pV6Z level of theory corrected by higher coupled-cluster level contributions.⁵¹ Panel B: Experimentally observed isotherms in the pVT diagram for pure xenon (dashed lines)²⁸ and computed pVT state points (full circles) with optimized LJ parameters.

absolute RMSE of 124.3 Pa) when using the original parameters.⁵⁰

Figure 1B compares the Xe-Xe interaction based on a LJ potential using the optimized LJ parameters and those from Aziz *et al.*. The dissociation energies are 0.450 kcal/mol and 0.561 kcal/mol, respectively, at equilibrium separations of $r_e = 4.31$ Å and 4.36 Å. This compares with a dissociation energy of 0.556 kcal/mol and $r_e = 4.40$ Å from high-level CCSD(T)/cc-pV6Z calculations.⁵¹ The zero point vibrational energy for a xenon pair is found to be 10.4 cm^{-1} (0.030 kcal/mol) experimentally⁵² and 0.029 kcal/mol computationally using

the CCSD(T)/cc-pV6Z potential data and a 1-dimensional DVR method.⁵¹

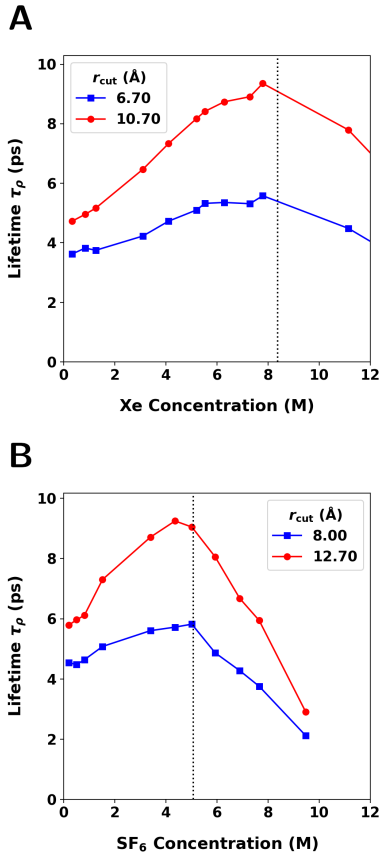


Figure 2: Local solvent reorganization lifetime τ_ρ from MD simulations of pure (A) Xenon at $T = 291.2 \text{ K}$ and (B) SF_6 system at $T = 321.9 \text{ K}$. The cutoff radii of the local solvent clusters are determined from the local minima in the respective radial distribution functions. The vertical dotted line marks the experimentally determined critical concentration at the critical temperatures of $c(\text{Xe}) = 8.45 \text{ M}$ and $c(\text{SF}_6) = 5.02 \text{ M}$, respectively.²⁷

Following previous work,²¹ the local solvent reorganization lifetime τ_ρ was used to probe for distinct SCF properties and as a proxy to determine the computationally predicted critical density at the given temperature, following established routes.^{53,54} Figures 2A and B show the computed τ_ρ for liquid xenon and SF_6 , respectively. For the analysis, the cutoff radii for the first and second solvation shells of a local solvent residue cluster were estimated from the local minima of the respective radial distribution function $g(r)$ determined from the same trajectory. For both solvents, the maxima of τ_ρ for the simulated solvent concentration

are close to the experimentally observed critical concentrations at the critical temperature. As was found in previous work,^{53,54} the solvent fluctuation lifetime, τ_ρ , in LJ gas systems is a maximum for supercritical fluids at the critical concentration. This indicates that the supercritical dynamical properties are well captured by the solvent potential model and are one more manifestation of critical slowing, at least in pure xenon and SF₆.

Intermolecular Interactions: The intermolecular interactions between the N₂O solute and the Xe or SF₆ solvent were fit to reproduce counterpoise corrected *ab initio* reference interaction energies for various solute-solvent clusters. Figures 3A and B show the correlation between the modelled and reference interactions for optimized LJ parameter of the N₂O atoms, respectively. The solute-solvent clusters with N₂O at their center have a maximum radius of 6.5 Å for Xe and 7.5 Å for SF₆, respectively. The number of solvent atoms or molecules within the cluster are representative for the local density of gaseous, supercritical and liquid solvent environments, respectively, and the selection of cluster conformations are described in the Method section.

The N₂O–Xe interaction in Figure 3A with optimized LJ parameter for N₂O reproduces the reference interaction energies with RMSEs from gaseous to liquid-like solvent clusters with 0.17, 0.27 and 0.30 kcal/mol, respectively. In contrast, for the N₂O–SF₆ interactions (see Figure 3B) the RMSEs increase to 0.29, 0.79 and 1.13 kcal/mol, respectively. The interactions in supercritical and liquid-like cluster environments with $n = 6$ and 10 SF₆ molecules are overestimated due to stronger electrostatic interactions compared with Xe.

Rotational Energy Relaxation (RER)

From the simulations the N₂O atom positions and velocities were recorded every 50 fs from the aggregate of 50 ns (5×10 ns) for each system and composition. The RER rates $1/\tau_{\text{rot}}$ were

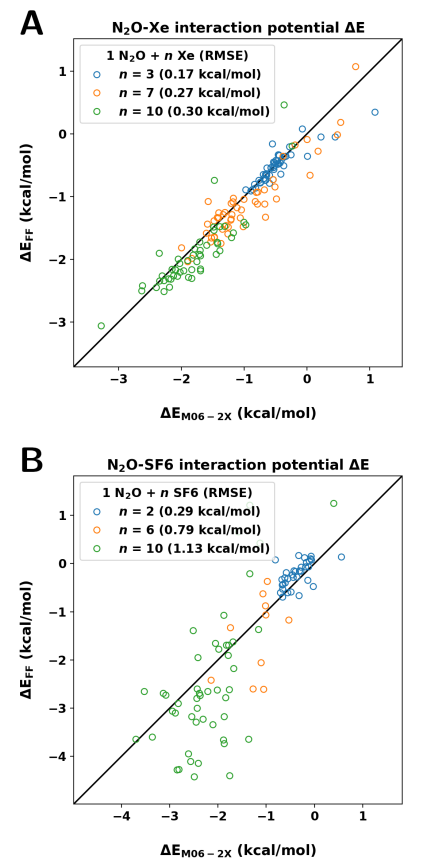


Figure 3: Correlation plot of the optimized interaction potential model against the *ab initio* reference interaction energies between N₂O within (A) xenon and (B) SF₆ solvent clusters of different densities. The number of solvent particles in the cluster are given in the respective legend, respectively.

then determined from the $E_{\text{rot}}(t)$ autocorrelation function by fitting to a single-exponential function (see Equation 4), yielding a single RER time τ_{rot} . Figure 4 shows RER rates in xenon and SF₆ retrieved from the corresponding calculated rotational energy correlation functions, see Figures S1 and S2.

As an extension, a bi-exponential function was used to fit the rotational energy correlation functions. This yields two time scales: fast and a slow RER times $\tau_{\text{rot,fast}}$ and $\tau_{\text{rot,slow}}$ shown in Figure S3. In general, τ_{rot} from the single-exponential fit matches the slow component of the RER time $\tau_{\text{rot,slow}}$ from which the respective rates are closest to the experimental results. Thus, only the fit parameters of the single-exponential function will be discussed.

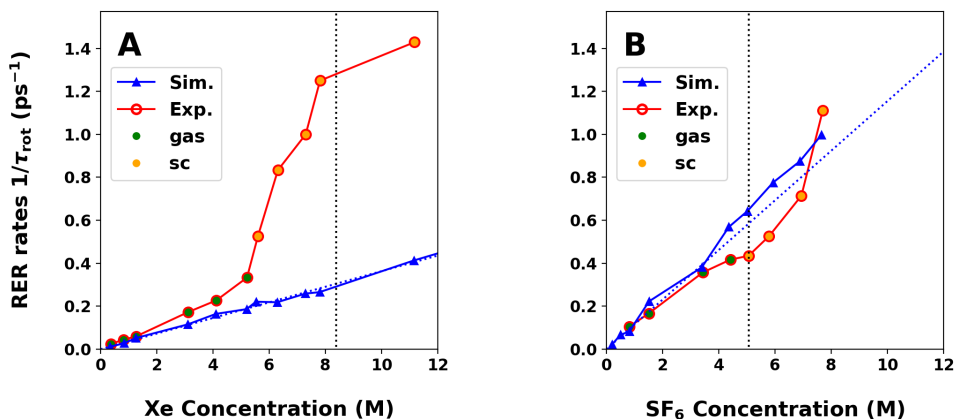


Figure 4: RER rates from the RER times τ_{rot} of a fitted single-exponential function to correlation function of the rotational energy $E_{\text{rot}}(t)$ of N_2O in (A) xenon and (B) SF_6 at different solvent concentrations (solid blue lines). The solid red line with colored circle markers shows the experimentally measured RER rates and indicate the solvent state gaseous or supercritical (sc).²⁰ The dotted blue line is an linear extrapolation of the first 3 simulated RER rates. The vertical dotted lines mark the experimentally observed solvent concentration at the respective critical density of xenon and SF_6 , respectively.

Analysis of the 2D IR experiments provided RER rates for N_2O molecules in gaseous, supercritical and liquid solvent regions.^{18–20} For xenon a characteristic increase in $1/\tau_{\text{rot}}$ for $c[\text{Xe}] > 4$ M was found whereas for SF_6 critical slowing for $c[\text{SF}_6] > 4$ M was observed (red traces in Figures 4A and B). Both measurements deviate from results predicted by the simplest IBC model which predicts a linear dependence between $c[\text{solvent}]$ and $1/\tau_{\text{rot}}$. From the simulations in xenon, however, the results follow that expected from IBC (blue symbols in Figure 4A) whereas for SF_6 the computed results deviate around the predictions from IBC, see Figure 4B.

The agreement between computed RER rates and the IBC model rather than the experimentally observed RER rates at supercritical solvent concentrations becomes apparent when scaling the rates with the concentration to yield the RER rates k_{rot} . From the slopes of the RER rate dependence of the IBC region in the Figure 4, the simulated N_2O RER rates

are $k_{\text{rot}}^{\text{Xe}} = (3.67 \pm 0.25) \cdot 10^{10} \text{ s}^{-1}\text{M}^{-1}$ and $k_{\text{rot}}^{\text{SF}_6} = (1.25 \pm 0.12) \cdot 10^{11} \text{ s}^{-1}\text{M}^{-1}$ for N_2O in Xe and SF_6 , respectively. 2DIR derived measured RER rates for N_2O in gaseous xenon and SF_6 solvent within the IBC region are $5.36 \cdot 10^{10} \text{ s}^{-1}\text{M}^{-1}$ and $1.02 \cdot 10^{11} \text{ s}^{-1}\text{M}^{-1}$, respectively, which are rather close to the simulation results.²⁰ The ratio $k_{\text{rot}}^{\text{SF}_6}/k_{\text{rot}}^{\text{Xe}} \sim 3$ also qualitatively agrees with a factor of ~ 2 from the experiments.

Up to this point the rotational energy was used to determine the correlation function and to obtain RER rates. To probe whether other angular-momentum-dependent quantities lead to similar conclusions, correlation functions for N_2O angular momentum $\vec{L}(t)$, and the squared angular momentum $|L(t)|^2$ were considered, see Figures S4 and S5. Using $\vec{L}(t)$ yields higher rates than those from the squared angular momentum $|L(t)|^2$ which in turn closely matches the rates based on the rotational energy correlation function. This is not unexpected as the rotational energy is proportional to the squared angular momentum: $E_{\text{rot}}(t) = |L(t)|^2/(2I)$ with I the N_2O moment of inertia. The rates from $\vec{L}(t)$ are higher as they also include the reorientation of the rotational axis of N_2O known as rotational Brownian motion.⁵⁵

The respective correlation functions for $\vec{L}(t)$ and $|L(t)|^2$ of N_2O in xenon and SF_6 are shown in Figures S6 to S9. The correlation functions are the average of the correlation functions computed from each single sample run at the respective solvent concentration. RER rates from fits to the correlation functions of the angular momentum $\vec{L}(t)$, squared angular momentum $|\vec{L}(t)|^2$ and rotational energy E_{rot} are shown in Figures S10 and S11.

To conclude, for low solvent densities ($c[\text{Xe}] < 4 \text{ M}$ and $c[\text{SF}_6] < 4 \text{ M}$) the computed RER rates agree very favourably with experiments whereas for higher densities the deviations from the IBC model observed in the experiments are not correctly captured, specifically for xenon. Rather, the simulations follow the predicted behaviour from the IBC model. As the deviations are systematic with increasing solvent concentration it is conjectured that as the

solvent concentration increases the property probed by the experiment is not only the solute rotational energy. This is discussed further below. In addition, many-body effects may be insufficiently accounted for in the computational model, thus contributing to the lack of quantitative agreement particularly for N₂O in xenon at higher density.

Collision Analysis

The computed RER of N₂O in Xe and SF₆ followed the simple IBC model and is in disagreement with the experimentally observed rapid increase around $c[\text{Xe}] > 5 \text{ M}$ and critical slowing at the critical density for SF₆. To gain deeper insight into the solute-solvent interactions, the change in kinetic energy before and after N₂O-solvent collisions was further analyzed and decomposed into translational, rotational, and vibrational contributions of N₂O at different solvent densities.

Figure 5 shows the average absolute change in the kinetic energies of N₂O, xenon atoms and SF₆ molecules upon collision. A collision between N₂O and solvent was considered to have occurred when any of the N₂O-Xe or N₂O-SF₆ atom separations is smaller than the sum of their atomic van-der-Waals radii (1.55, 1.52, 2.16, 1.80, 1.47 Å for N, O, Xe, S and F, respectively).⁵⁶ The initial and final kinetic energies of N₂O and solvent were extracted from the simulation at the frame after crossing this van-der-Waals radii threshold from which the changes $|\Delta\bar{T}_\alpha|$ for $\alpha = \text{total, vib, rot, trans}$ and corresponding distributions $P(|\Delta\bar{T}_\alpha|)$ were determined. Due to intramolecular energy flow and intermolecular exchange of kinetic energy between the solute and the surrounding solvent molecules during the contact time, the sum of changes in the kinetic energy contributions does not necessarily add up to the total kinetic energy difference.

Related to RER are changes in the N₂O rotational kinetic energy, $|\Delta\bar{T}_{\text{rot}}|$, see Figures 5A

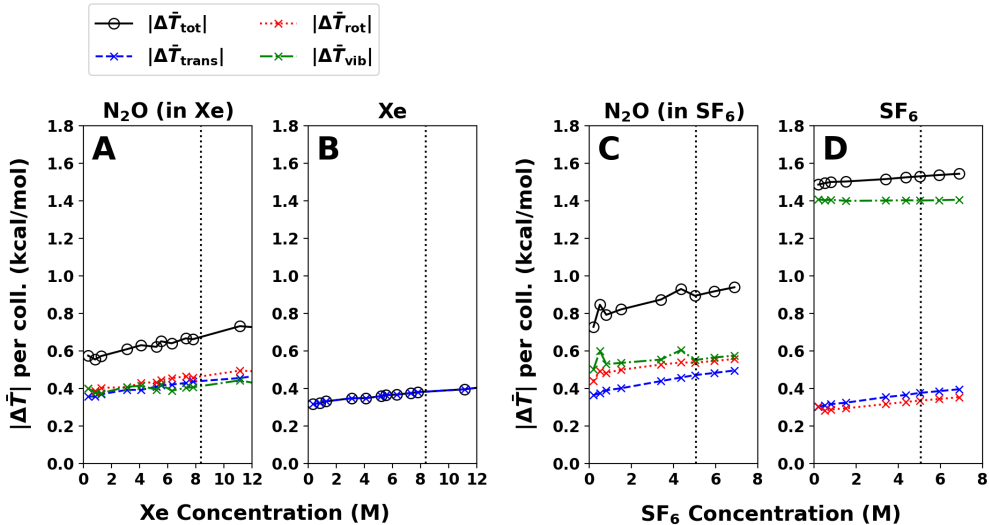


Figure 5: Averaged absolute energy difference $|\Delta\bar{T}|$ of the total, translational, rotational and vibrational kinetic energy after a collision between (A-B) N_2O and xenon, and (C-D) N_2O and SF_6 , respectively, at different solvent concentrations. The vertical dotted lines mark the experimentally observed solvent concentration at the respective critical density. Note the different system temperatures of 291.2 K and 321.9 K for N_2O in xenon and SF_6 , respectively.

and C (red dotted line). For N_2O in Xe, $|\Delta\bar{T}_{\text{rot}}|$ is lower than in SF_6 which indicates that in simulations with SF_6 as the solvent the change in the N_2O rotational energy occurs not only due to collisions as for xenon. Rather, RER is also influenced by the longer-ranging, anisotropic intermolecular interactions between N_2O and the nonvanishing higher-order multipoles of SF_6 . As the average change in vibrational kinetic energy in $|\Delta\bar{T}_{\text{vib}}|$ (dash-dotted green line) of N_2O is larger in SF_6 than in xenon, the overall change in total kinetic energy $|\Delta\bar{T}_{\text{tot}}|$ (solid black line) is considerably larger, whereas the changes in translational kinetic energy $|\Delta\bar{T}_{\text{trans}}|$ (dashed blue line) for the two solvents are comparable because the masses of xenon (131.3 u) and SF_6 (146.1 u) are similar.

The change in the kinetic energy contributions of the solvent particles, xenon and SF_6 , after a collision with N_2O are shown in Figures 5B and D. At an atomistic level the kinetic energy of a single xenon atom only consists of the translational contribution. Again, the

translational contributions for xenon and SF₆ are comparable (blue symbols in Figures 5B and D) due to their similar masses. However, because SF₆ has internal degrees of freedom, additional rotational and vibrational kinetic energy contributions arise and the total $|\Delta\bar{T}_{\text{tot}}|$ (open circles) for collisions with SF₆ are considerably larger than those of xenon. For SF₆ the rotational and translational contributions are similar in magnitude $|\Delta\bar{T}_{\text{rot}}| \sim |\Delta\bar{T}_{\text{trans}}|$ whereas $|\Delta\bar{T}_{\text{vib}}|$ is significantly larger. This is due to the larger number of vibrational degrees of freedom (15) compared with rotation (3) and translation (3). It is also interesting to note that the translational and rotational contributions for SF₆ depend on solvent-concentration whereas the vibrational contribution does not. This is consistent with the analysis of the experimental data which indicates that vibrational relaxation through intramolecular energy relaxation upon collision is IBC-like as opposed to rotational relaxation.²⁰

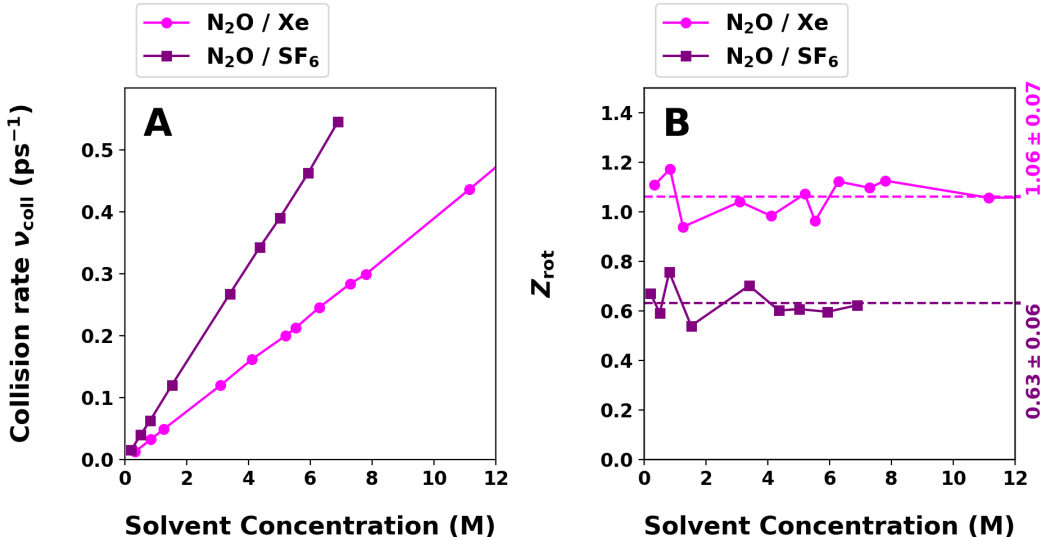


Figure 6: Panel A: Average collision rates ν_{coll} between N₂O and xenon (magenta) and SF₆ (purple) according to the collision conditions using atom distances and van-der-Waals radii thresholds defined for this work. Panel B: Average Number of collisions Z_{rot} for rotational relaxation of N₂O in xenon and SF₆ in the average and standard deviation displayed on the right axis.

Based on the RER rates $1/\tau_{\text{rot}}$ determined in the previous subsection and the average collision

frequency $\nu_{\text{coll}} = N_{\text{coll}}/t_{\text{sim}}$ ($t_{\text{sim}} = 50$ ns) it is also possible to compute the average number of collisions $Z_{\text{rot}} = \tau_{\text{rot}} \cdot \nu_{\text{coll}}$ required to rotationally relax the solute (N_2O). Here, N_{coll} is the number of collisions between N_2O and either xenon or SF_6 , and $1/\tau_{\text{rot}}$ was already obtained from fitting a single-exponential decay to the rotational energy correlation function of N_2O in both solvents. Figure 6A and B shows the computed average collision rate ν_{coll} and number of collision Z_{rot} for RER of N_2O in xenon and SF_6 , respectively. The collision rate of N_2O with SF_6 (purple line in Figure 6A) is higher than with xenon (magenta line) because of the higher simulation temperature (321.9 K vs. 291.2 K), the larger molecular volume occupied by SF_6 compared to a single xenon atom (based on atomic van der Waals radii), and the anisotropic electrostatic intermolecular interactions between N_2O and SF_6 .

The experimentally reported $Z_{\text{rot}}^{\text{expt}}$ are 2.4 and 1.7 for RER of N_2O in xenon and SF_6 , respectively, based on a hard sphere model for both types of solvent molecules.^{20,57} Within the IBC regime ($c[\text{Xe}] < 4$ M and $c[\text{SF}_6] < 4$ M) the $Z_{\text{rot}}^{\text{expt}}$ are larger than those from simulations. This is mostly due to the higher computed collision rate ν_{coll} , estimated from the inverse of the mean free collision time. On the other hand, the ratio $Z_{\text{rot}}^{\text{expt,Xe}}/Z_{\text{rot}}^{\text{expt,SF}_6}$ is comparable but somewhat smaller (~ 1.4) than that from the simulations (~ 1.7). This is also related to lower simulated RER rates for N_2O in xenon within the IBC region compared with experiments for which the simulated RER rates for N_2O in SF_6 matches well. Thus, the simulations reasonably well agree with the experiments for RER of N_2O over solvent concentrations within the IBC regime. However, the simulations do not reproduce the steep increase or critical slowing in the RER rates in xenon and SF_6 , respectively (see Figure 4).

Vibrational Energy Relaxation

VER lifetimes and rates were determined from the Landau-Teller formalism described in the Methods section. VER of a particular N_2O mode can either involve pure intramolecular

relaxation or a combination of inter- and intramolecular processes, both of which can be obtained from MD simulations.^{41–45} For this, the forces acting on the solute atoms derived only from the non-bonding solute-solvent interaction potential were extracted and projected along the normal mode vector of the asymmetric stretch vibration ν_{as} of N_2O , see Eq. 8.

For N_2O in SF_6 and from the experimental analysis,²⁰ the most effective vibrational relaxation channel of $\nu_{\text{as}}^{\text{N}_2\text{O}} \sim 2220 \text{ cm}^{-1}$ occurs through coupling with the symmetric N_2O stretch vibration $\nu_{\text{s}}^{\text{N}_2\text{O}} \sim 1280 \text{ cm}^{-1}$ and the three-fold degenerate S–F stretch vibration $\nu_3^{\text{SF}_6} \sim 948 \text{ cm}^{-1}$. Following the procedure outlined in the methods section, the VER rate for $(\nu_{\text{s}}, \nu_{\text{as}}) = (0, 1) \rightarrow (1, 0)$ were computed. The forces of N_2O are projected along the normal mode vectors of ν_{as} obtained from instantaneous normal mode analysis at the respective frames, which can be interpreted as solvent friction. The Fourier transform of the correlation function of this quantity yields the frequency dependent friction function, see Figures S16 and S17.

The VER lifetimes τ_{vib} for the relaxation $(0, 1) \rightarrow (1, 0)$ in N_2O were determined by the average of the friction function weighted by the frequency difference distribution $P(\nu_{\text{as}} - \nu_{\text{s}})$. The resulting rates $1/\tau_{\text{vib}}$ from simulation and experiments²⁰ are shown in Figure 7. The average frequency difference in the simulation were determined to be $\Delta\nu_{\text{model}} = 886 \text{ cm}^{-1}$ but $\Delta\nu_{\text{exp}} = 940 \text{ cm}^{-1}$ in experiments.²⁰ For consistency, the same distribution width centered around the experimentally observed frequency difference $\Delta\nu_{\text{exp}}$ was used to compute the τ_{vib} (see green dashed line in Figure 7B).

For N_2O in xenon, the computed N_2O VER rates for ν_{as} in Figure 7A are on the ns^{-1} time scale for supercritical xenon and indicate a rather slow VER relaxation process, as expected, with an average VER rate of $k_{\text{VER}} = (3.52 \pm 0.15) \cdot 10^8 \text{ s}^{-1}\text{M}^{-1}$. Experimentally,²⁰ a VER rate of $k_{\text{VER}} \approx 5.1 \cdot 10^7 \text{ s}^{-1}\text{M}^{-1}$ ($\approx 8.5 \cdot 10^{-14} \text{ cm}^3\text{s}^{-1}$) was indirectly obtained from a small ($\sim 5\%$) reduction of the pump-probe decay signal within 200 ps which corresponds to $\tau_{\text{vib}} \approx 2.5 \text{ ns}$ but

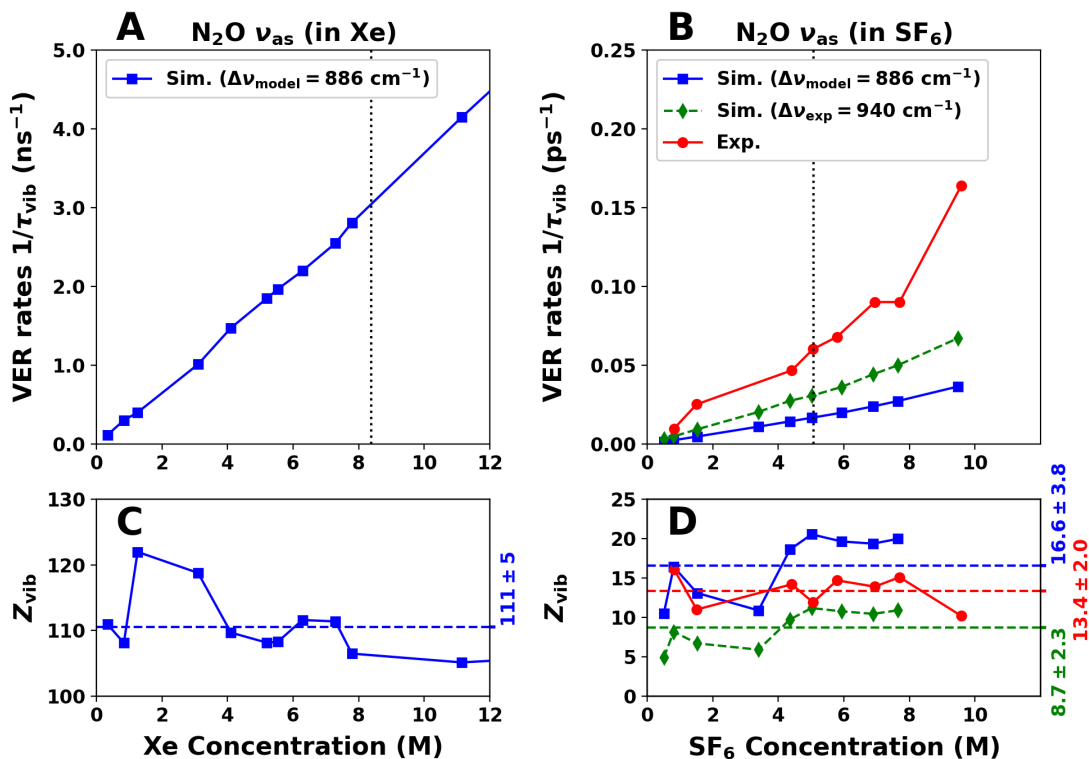


Figure 7: Computed VER rates (blue squares) for $(\nu_s, \nu_{as}) = (0, 1) \rightarrow (1, 0)$ with frequency difference $\Delta\nu = \nu_{as} - \nu_s$ computed from the frequency dependent friction function of the asymmetric stretch vibration of N_2O in (A) xenon and (B) SF_6 solvent at different solvent densities.^{41,42} The frequency difference $\Delta\nu$ is given in the legend in brackets. For N_2O in SF_6 (B), experimental values are available from Ref. 20 and VER rates are shown in assumption that $\Delta\nu$ matches the experimentally observed transition frequency of N_2O in SF_6 (green diamonds). Note the different unit representation of the VER rates in panels A and B. The vertical dotted lines mark the experimentally observed solvent concentration at the respective critical density of xenon and SF_6 , respectively. Panels C and D show the computed (and experimentally observed) number of collision Z_{vib} for the vibrational relaxation of N_2O with average and standard deviation displayed on the right axis.

was only measured at high xenon concentration (7.8 M). This compares with $k_{\text{VER}} = 3.47 \cdot 10^8 \text{ s}^{-1}\text{M}^{-1}$ from the simulations which is ~ 7 times faster compared with the estimate from the experiments. It should be noted that the Landau-Teller model was successfully applied to rather long VER times ($\sim 600 \text{ ps}$) for the case of CO in myoglobin.⁴⁴ Hence it is likely that the Landau-Teller approach for VER is valid but the limitations for N_2O in xenon arise due to neglect of many-body interactions, in particular at high solvent densities but also due to

the uncertainty in the measurements.

On the other hand, for N₂O in SF₆ (panel B), the computed VER rates obtained with the model frequency difference distribution around $\Delta\nu_{\text{model}}$ (blue line) are on the ps⁻¹ time scale for gaseous and supercritical SF₆. Assuming a frequency difference distribution around the experimental value $\Delta\nu_{\text{exp}}$ the VER rates are higher by a factor of two (green dashed line). The VER of $\nu_{\text{as}}^{\text{N}_2\text{O}}$ is faster in SF₆ than in xenon due to the coupling with three-times degenerated the S-F stretch modes at $\nu_3 = 948 \text{ cm}^{-1}$, which is well visible by a peak around this wavenumber in the friction function in Figure S17.

The available experimental data of the VER rates for N₂O ν_{as} in SF₆ (red circles in Figure 7B) are still about four or two times faster than VER rates computed with the frequency difference distribution from the model simulation or experimental observations, respectively. The computed VER rates, however, feature a linear raise with increasing SF₆ concentration which corresponds to VER rates of $k_{\text{VER}}(\Delta\nu_{\text{exp}}) = (3.31 \pm 0.27) \cdot 10^9 \text{ s}^{-1}\text{M}^{-1}$ and $k_{\text{VER}}(\Delta\nu_{\text{exp}}) = (6.28 \pm 0.32) \cdot 10^9 \text{ s}^{-1}\text{M}^{-1}$. The experimentally reported VER rate for N₂O ν_{as} in gaseous SF₆ or the IBC regime is $k_{\text{VER,IBC}} = 1.56 \cdot 10^{10} \text{ s}^{-1}\text{M}^{-1}$ ($2.6 \cdot 10^{-11} \text{ cm}^3\text{s}^{-1}$).²⁰

Scaling the computed VER lifetimes τ_{vib} with the estimated collision rate τ_{coll} reveals that for N₂O in xenon an average of $Z_{\text{vib}} = \tau_{\text{vib}} \cdot \tau_{\text{coll}} = 111 \pm 5$ collisions between N₂O and xenon atoms are required to relax the asymmetric stretch vibration in N₂O. Using the experimentally estimated τ_{vib} would yield a yet larger value for Z_{vib} by one order of magnitude. For N₂O in SF₆, $Z_{\text{vib}}(\text{SF}_6) = 16.6 \pm 3.8$ or 8.7 ± 2.3 is about one order of magnitude smaller depending on whether $\Delta\nu_{\text{model}}$ or $\Delta\nu_{\text{exp}}$ are used for estimating the VER lifetime, respectively. From experiments, $Z_{\text{vib}}^{\text{expt.}} = 13.4 \pm 2.0$ collisions between N₂O and SF₆ are required. This is midway between the two computed values due to differences in the estimated collision rate. The collision rate from the estimated mean free collision time - which is larger than the one

obtained from counting collision events - together with the underestimated VER rate lead to closer agreement of computed and experimentally estimated Z_{vib} than comparison of the VER.

Even if VER rates from simulations are computed using the experimentally reported frequency difference $\Delta\nu_{\text{exp}}$, the VER rates are still half as fast compared with the experimentally measured VER rates for N_2O in SF_6 . The first-order Landau-Teller model to compute the VER lifetimes used here only includes the term describing solvent friction, i.e. the influence of the solute-solvent interaction potential V_{int} on the normal mode $\nu_{\text{as}}^{\text{N}_2\text{O}}$. Shorter lifetimes might be obtained by including higher-order correction terms such as solvent-induced coupling to the solute-solvent interaction potential expression in Eq. 8. Such terms include the second derivative of V_{int} along the solute normal mode of $\nu_{\text{as}}^{\text{N}_2\text{O}}$ and $\nu_{\text{s}}^{\text{N}_2\text{O}}$ describing the relaxation pathway of intramolecular VER assisted by the solvent.⁴³

Discussion and Conclusions

The present work provides a atom-resolved picture of rotational and vibrational energy relaxation of N_2O in xenon and SF_6 covering a wide range of thermodynamic states ranging from the gas phase to the liquid. In an effort to improve the solvent-solute interactions, the electrostatic and other nonbonded interactions were fit to reference electronic structure calculations at different levels of theory. While for VER satisfactory results compared with experiment were found, RER agrees with experiment only up to $c[\text{solvent}] \sim 4$ M. For higher concentrations the simulation follow the IBC model whereas experimentally different behaviours are found for xenon and SF_6 .

For N_2O in xenon the experiments find a pronounced increase in the RER time as the concentration increases from 6 M to 8 M, see Figure S4. The experiments are expected to

report on the solvent rotational energy normalized autocorrelation function $\langle E_{\text{rot}}(0)E_{\text{rot}}(t) \rangle$. For low-density solvent the experimental result could be reproduced almost quantitatively, whereas for increasing density no discontinuous change of the RER time was found. Rather, the linear behaviour - consistent with the IBC model - continued up to the highest simulated densities yield RER rates of $(3.67 \pm 0.25) \cdot 10^{10} \text{ s}^{-1}\text{M}^{-1}$ and $(1.25 \pm 0.12) \cdot 10^{11} \text{ s}^{-1}\text{M}^{-1}$ for N_2O in xenon and SF_6 , respectively. These computed RER rates agree well with those from experiment within the IBC region of $5.36 \cdot 10^{10} \text{ s}^{-1}\text{M}^{-1}$ and $1.02 \cdot 10^{11} \text{ s}^{-1}\text{M}^{-1}$, respectively.

In search for a reason for the disagreement, additional correlation functions, including $\langle \vec{L}_{\text{N}_2\text{O}}(0)\vec{L}_{\text{N}_2\text{O}}(t) \rangle$, $\langle E_{\text{rot,N}_2\text{O}}(0)E_{\text{rot,N}_2\text{O}}(t) \rangle$, and $\langle \mu_{\text{N}_2\text{O}}(0)\mu_{\text{N}_2\text{O}}(t) \rangle$ were analyzed. However, all of them confirm the behaviour of the computed $\langle \vec{L}_{\text{N}_2\text{O}}^2(0)\vec{L}_{\text{N}_2\text{O}}^2(t) \rangle$ correlation function. One possible explanation for this finding is to note that with increasing density the solvent packing around the solute becomes so dense, that the isolated N_2O properties ($E_{\text{rot,N}_2\text{O}}$ or $\vec{L}_{\text{N}_2\text{O}}$) cannot be compared with the experimentally observed signals. The rotation of N_2O cannot be treated isolated from the movement of the solvation shells. Rather, for sufficiently large solvent densities the rotational motion of N_2O and the solvent molecules are coupled and solvent molecules are “slaved” to the N_2O rotation. Quantum-mechanically, the rotational quantum number correlating with $\vec{L}_{\text{N}_2\text{O}}$ is a “good quantum number” for gas phase and low solvent densities whereas this property is lost for increasing solvent density.

Analysis of the trajectories with regards to changes in kinetic energy (squared momentum transfer) between the collision partners (N_2O and xenon; N_2O and SF_6) revealed a larger average change for the rotational energy of N_2O when colliding with SF_6 than with xenon. The translational kinetic energy change of the solvent molecules xenon and SF_6 are comparable, whereas the additional rotational and vibrational degrees of freedom in SF_6 provide further energy transfer pathways compared with xenon.

Considering RER, the average number of collisions to rotationally relax N_2O over the concentration range considered are $Z_{\text{rot}}^{\text{Xe}} = 1.1$ and $Z_{\text{rot}}^{\text{SF}_6} = 0.6$, respectively. This shows that RER for N_2O in SF_6 is about ~ 1.7 times more effective than in xenon, which is consistent with experiments. There, the values of 2.4 and 1.7 collision are about 2 to 3 times larger for SF_6 compared with xenon, indicating a less efficient rotational relaxation per collision in the simulations. The largest deviations between experiments and the simulations are in the collision rates which are twice as high when estimated from the inverse of the mean free collision times. Together with the simulated RER rates this yields Z'_{rot} of 2.5 and 1.4 for N_2O in xenon and SF_6 , respectively, which is much closer to the experiments. The relative change $|\Delta\bar{T}_{\text{rot}}^{\text{SF}_6}|/|\Delta\bar{T}_{\text{rot}}^{\text{Xe}}|$ is somewhat smaller but comparable to $|\Delta\bar{T}_{\text{vib}}^{\text{SF}_6}|/|\Delta\bar{T}_{\text{vib}}^{\text{Xe}}|$ depending on solvent concentration which indicates that angular anisotropy of the intermolecular interactions influence RER.

Values of the VER rates are computed by the Landau-Teller approach and show a very slow VER process of the asymmetric stretch vibration ν_{as} of N_2O in xenon with a VER rate of $(3.52 \pm 0.15) \cdot 10^8 \text{ s}^{-1}\text{M}^{-1}$. In SF_6 , the computed rates are much faster by one magnitude with $(3.31 \pm 0.27) \cdot 10^9 \text{ s}^{-1}\text{M}^{-1}$ or $(6.28 \pm 0.32) \cdot 10^9 \text{ s}^{-1}\text{M}^{-1}$ depending on the applied frequency difference distribution $P(\nu_{\text{as}} - \nu_{\text{s}})$ for the relaxation process $(\nu_{\text{s}}, \nu_{\text{as}}) = (0, 1) \rightarrow (1, 0)$. These rates are about four or two times lower than the experimentally observed VER rate in the IBC regime at low solvent densities of $1.56 \cdot 10^{10} \text{ s}^{-1}\text{M}^{-1}$, but also do the computed VER rates of N_2O ν_{as} in SF_6 around its critical density not show the effect of critical slowing as in the experiments (see Figure 7B). This deficiency of the simulation, however, is consistent with the missing effect of critical slowing in the computed RER rates for N_2O in SF_6 .

In summary, this work presented a molecular-level study of rotational and vibrational energy relaxation of N_2O in xenon and SF_6 ranging from highly dilute to liquid phases of the solvent, including the supercritical regime. For regimes in which the IBC model is valid almost

quantitative agreement with experiment was found whereas near the supercritical point simulations and experimental findings disagree, in particular for RER. The most likely reason is that the effect of solvent packing is neglected in the analysis if only the rotational motion of the solute (N_2O) is considered. The average number of collisions for rotational and vibrational relaxation from the simulations agree rather well with those obtained from experiments. In conclusion, VER of N_2O across different solvent density regimes and RER in the low-density region can be characterized well at a molecular level whereas for the higher-density regimes, analysis of the RER requires additional refinements.

Acknowledgment

This work has been financially supported by the Swiss National Science Foundation (NCCR-MUST, grants 200021-117810, 200020-188724), the AFOSR, the University of Basel, and by the European Union’s Horizon 2020 research and innovation program under the Marie Skłodowska-Curie grant agreement No 801459 -FP-RESOMUS. The support of the National Science Foundation, Grant No. CHE-2102427 (L.D.Z.), and the Boston University Photonics Center is gratefully acknowledged.

Supporting Information

The supporting material includes system setups (Table S1), force field parameters (Table S2), various correlation functions (Figures S1, S2, S6-S9) with further evaluation results (Figures S3-S5, S10-S15) and the frequency-dependent friction functions (Figures S16, S17).

Data Availability

Relevant data for the present study are available at https://github.com/MMunibas/SCF_N20/.

References

- (1) Foster, J.; Miller, R. S. *High Pressure Processes in Chemical Engineering*; pp 53–75.
- (2) Guardiola, C.; Olmeda, P.; Pla, B.; Bares, P. In-cylinder pressure based model for exhaust temperature estimation in internal combustion engines. *Appl. Therm. Eng.* **2017**, *115*, 212–220.
- (3) Farrell, P. V.; Peters, B. D. Droplet vaporization in supercritical pressure environments. *Acta Astronaut.* **1986**, *13*, 673–680, Congress of the International Academy of Astronautics.
- (4) Kajimoto, O. Solvation in Supercritical Fluids: Its Effects on Energy Transfer and Chemical Reactions. *Chem. Rev.* **1999**, *99*, 355–*390.
- (5) Knez, Ž.; Markočič, E.; Leitgeb, M.; Primožič, M.; Knez Hrnčič, M.; Škerget, M. Industrial applications of supercritical fluids: A review. *Energy* **2014**, *77*, 235–243.
- (6) Brunner, G. Applications of Supercritical Fluids. *Annu. Rev. Biomed. Eng.* **2010**, *1*, 321–342.
- (7) Hrnčič, M. K.; Cör, D.; Verboten, M. T.; Knez, Ž. Application of supercritical and subcritical fluids in food processing. *Food Qual. Saf.* **2018**, *2*, 59–67.
- (8) Perrut, M. Supercritical Fluid Applications: Industrial Developments and Economic Issues. *Industrial & Engineering Chemistry Research* **2000**, *39*, 4531–4535.

- (9) Deshpande, P. B.; Kumar, G. A.; Kumar, A. R.; Shavi, G. V.; Karthik, A.; Reddy, M. S.; Udupa, N. Supercritical Fluid Technology: Concepts and Pharmaceutical Applications. *PDA Journal of Pharmaceutical Science and Technology* **2011**, *65*, 333–344.
- (10) Machida, H.; Takesue, M.; Smith, R. L. Green chemical processes with supercritical fluids: Properties, materials, separations and energy. *The Journal of Supercritical Fluids* **2011**, *60*, 2–15.
- (11) Tucker, S. C. Solvent Density Inhomogeneities in Supercritical Fluids. *Chem. Rev.* **1999**, *99*, 391–418.
- (12) Saitow, K.; Otake, K.; Nakayama, H.; Ishii, K.; Nishikawa, K. Local density enhancement in neat supercritical fluid due to attractive intermolecular interactions. *Chem. Phys. Lett.* **2003**, *368*, 209–214.
- (13) Nishikawa, K.; Morita, T. Inhomogeneity of molecular distribution in supercritical fluids. *Chem. Phys. Lett.* **2000**, *316*, 238–242.
- (14) Saitow, K.-i.; Ochiai, H.; Kato, T.; Nishikawa, K. Correlation time of density fluctuation for supercritical ethylene studied by dynamic light scattering. *J. Chem. Phys.* **2002**, *116*, 4985–4992.
- (15) Saitow, K.-i.; Kajiya, D.; Nishikawa, K. Time Evolution of Density Fluctuation in Supercritical Region. I. Non-hydrogen-bonded Fluids Studied by Dynamic Light Scattering. *J. Phys. Chem. A* **2005**, *109*, 83–91.
- (16) Goodyear, G.; Tucker, S. C. Glass-like behavior in supercritical fluids: The effect of critical slowing down on solute dynamics. *J. Chem. Phys.* **1999**, *111*, 9673–9677.
- (17) Goodyear, G.; Maddox, M. W.; Tucker, S. C. The correlation between local and long-range structure in compressible supercritical fluids. *J. Chem. Phys.* **2000**, *112*, 10327–10339.

- (18) Mandal, A.; Ng Pack, G.; Shah, P. P.; Erramilli, S.; Ziegler, L. D. Ultrafast Two-Dimensional Infrared Spectroscopy of a Quasifree Rotor: J Scrambling and Perfectly Anticorrelated Cross Peaks. *Phys. Rev. Lett.* **2018**, *120*, 103401.
- (19) Ng Pack, G.; Rotondaro, M. C.; Shah, P. P.; Mandal, A.; Erramilli, S.; Ziegler, L. D. Two-dimensional infrared spectroscopy from the gas to liquid phase: density dependent J -scrambling, vibrational relaxation, and the onset of liquid character. *Phys. Chem. Chem. Phys.* **2019**, *21*, 21249–21261.
- (20) Rotondaro, M. C.; Jain, A.; Erramilli, S.; Ziegler, L. D. Ultrafast 2DIR comparison of rotational energy transfer, isolated binary collision breakdown, and near critical fluctuations in Xe and SF₆ solutions. *J. Chem. Phys.* **2022**, *157*, 174305.
- (21) Töpfer, K.; Erramilli, D. K.; Ziegler, L. D.; Meuwly, M. Molecular-level understanding of the rovibrational spectra of N₂O in gaseous, supercritical, and liquid SF₆ and Xe. *J. Chem. Phys.* **2023**, *158*, 144302.
- (22) Unke, O. T.; Meuwly, M. Toolkit for the Construction of Reproducing Kernel-based Representations of Data: Application to Multidimensional Potential Energy Surfaces. *J. Chem. Inf. and Mod.* **2017**, *57*, 1923–1931.
- (23) Koner, D.; San Vicente Veliz, J. C.; Bemish, R. J.; Meuwly, M. Accurate reproducing kernel-based potential energy surfaces for the triplet ground states of N₂O and dynamics for the N + NO \leftrightarrow O + N₂ and N₂ + O \rightarrow 2N + O reactions. *Phys. Chem. Chem. Phys.* **2020**, *22*, 18488–18498.
- (24) Werner, H.-J.; Knowles, P. J.; Manby, F. R.; Black, J. A.; Doll, K.; Heßelmann, A.; Kats, D.; Köhn, A.; Korona, T.; Kreplin, D. A. et al. The Molpro quantum chemistry package. *J. Chem. Phys.* **2020**, *152*, 144107.
- (25) Dellis, D.; Samios, J. Molecular force field investigation for Sulfur Hexafluoride: A computer simulation study. *Fluid Phase Equilib.* **2010**, *291*, 81–89.

- (26) Stephenson, R. M.; Malanowski, S.; Ambrose, D. *Handbook of the thermodynamics of organic compounds; section on vapor-liquid critical constants of fluids*; Elsevier, 1987.
- (27) Haynes, W. *CRC Handbook of Chemistry and Physics*; CRC Handbook of Chemistry and Physics; CRC Press, 2014; p. 6-85.
- (28) Michels, A.; Wassenaar, T.; Louwerse, P. Isotherms of xenon at temperatures between 0°C and 150°C and at densities up to 515 Amagats (pressures up to 2800 atmospheres). *Physica* **1954**, *20*, 99–106.
- (29) Nelder, J. A.; Mead, R. A Simplex Method for Function Minimization. *Comput. J.* **1965**, *7*, 308–313.
- (30) Devereux, M.; Raghunathan, S.; Fedorov, D. G.; Meuwly, M. A Novel, computationally efficient multipolar model employing distributed charges for molecular dynamics simulations. *J. Chem. Theo. Comp.* **2014**, *10*, 4229–4241.
- (31) Unke, O. T.; Devereux, M.; Meuwly, M. Minimal distributed charges: Multipolar quality at the cost of point charge electrostatics. *J. Chem. Phys.* **2017**, *147*, 161712.
- (32) Devereux, M.; Pezzella, M.; Raghunathan, S.; Meuwly, M. Polarizable Multipolar Molecular Dynamics Using Distributed Point Charges. *J. Chem. Theo. Comp.* **2020**, *16*, 7267–7280.
- (33) Frisch, M. J.; Trucks, G. W.; Schlegel, H. B.; Scuseria, G. E.; Robb, M. A.; Cheeseman, J. R.; Scalmani, G.; Barone, V.; Petersson, G. A.; Nakatsuji, H. et al. Gaussian~16 Revision C.01. 2016; Gaussian Inc. Wallingford CT.
- (34) Olney, T. N.; Cann, N.; Cooper, G.; Brion, C. Absolute scale determination for photoabsorption spectra and the calculation of molecular properties using dipole sum-rules. *Chem. Phys.* **1997**, *223*, 59–98.

- (35) Gussoni, M.; Rui, M.; Zerbi, G. Electronic and relaxation contribution to linear molecular polarizability. An analysis of the experimental values. *J. Mol. Struct.* **1998**, *447*, 163–215.
- (36) Branch, M. A.; Coleman, T. F.; Li, Y. A Subspace, Interior, and Conjugate Gradient Method for Large-Scale Bound-Constrained Minimization Problems. *SIAM J Sci Comput* **1999**, *21*, 1–23.
- (37) Boys, S.; Bernardi, F. The calculation of small molecular interactions by the differences of separate total energies. Some procedures with reduced errors. *Molecular Physics* **1970**, *19*, 553–566.
- (38) Grimme, S.; Antony, J.; Ehrlich, S.; Krieg, H. A consistent and accurate ab initio parametrization of density functional dispersion correction (DFT-D) for the 94 elements H-Pu. *J. Chem. Phys.* **2011**, *132*, 154104.
- (39) Brooks, B. R.; Brooks III, C. L.; MacKerell Jr., A. D.; Nilsson, L.; Petrella, R. J.; Roux, B.; Won, Y.; Archontis, G.; Bartels, C.; Boresch, S. et al. CHARMM: The Biomolecular Simulation Program. *J. Comp. Chem.* **2009**, *30*, 1545–1614.
- (40) Martínez, L.; Andrade, R.; Birgin, E. G.; Martínez, J. M. Packmol: A Package for Building Initial Configurations for Molecular Dynamics Simulations. *J. Chem. Theo. Comp.* **2009**, *30*, 2157–2164.
- (41) Whitnell, R. M.; Wilson, K. R.; Hynes, J. T. Vibrational relaxation of a dipolar molecule in water. *J. Chem. Phys.* **1992**, *96*, 5354–5369.
- (42) Rey, R.; Hynes, J. T. Vibrational phase and energy relaxation of CN^- in water. *J. Chem. Phys.* **1998**, *108*, 142–153.
- (43) Morita, A.; Kato, S. Vibrational relaxation of azide ion in water: The role of intramolecular charge fluctuation and solvent-induced vibrational coupling. *J. Chem. Phys.* **1998**, *109*, 5511–5523.

- (44) Sagnella, D. E.; Straub, J. E.; Jackson, T. A.; Lim, M.; Anfinrud, P. A. Vibrational population relaxation of carbon monoxide in the heme pocket of photolyzed carbon-monooxy myoglobin: Comparison of time-resolved mid-IR absorbance experiments and molecular dynamics simulations. *Proc. Natl. Acad. Sci.* **1999**, *96*, 14324–14329.
- (45) Everitt, K. F.; Skinner, J. L. Vibrational energy relaxation of oxygen in liquid mixtures with argon. *J. Chem. Phys.* **1999**, *110*, 4467–4470.
- (46) Tennyson, J.; Kostin, M. A.; Barletta, P.; Harris, G. J.; Polyansky, O. L.; Ramanlal, J.; Zobov, N. F. DVR3D: a program suite for the calculation of rotation–vibration spectra of triatomic molecules. *Comput. Phys. Commun.* **2004**, *163*, 85–116.
- (47) Herzberg, G. *Infrared and Raman Spectra of Polyatomic Molecules*; D. Van Nostrand Company, Inc., New York, 1945.
- (48) Herzberg, G.; Herzberg, L. Rotation-Vibration Spectra of Diatomic and Simple Polyatomic Molecules with Long Absorbing Paths VI. The Spectrum of Nitrous Oxide (N_2O) below 1.2μ . *J. Chem. Phys.* **1950**, *18*, 1551–1561.
- (49) Kagann, R. H. Infrared absorption intensities for N_2O . *J. Mol. Spectrosc.* **1982**, *95*, 297–305.
- (50) Aziz, R. A.; Slaman, M. On the Xe-Xe potential energy curve and related properties. *Mol. Phys.* **1986**, *57*, 825–840.
- (51) Hellmann, R.; Jäger, B.; Bich, E. State-of-the-art ab initio potential energy curve for the xenon atom pair and related spectroscopic and thermophysical properties. *J. Chem. Phys.* **2017**, *147*, 034304.
- (52) Freeman, D. E.; Yoshino, K.; Tanaka, Y. Vacuum ultraviolet absorption spectrum of the van der Waals molecule Xe_2 . I. Ground state vibrational structure, potential well depth, and shape. *J. Chem. Phys.* **1974**, *61*, 4880–4889.

- (53) Maddox, M. W.; Goodyear, G.; Tucker, S. C. Origins of Atom-Centered Local Density Enhancements in Compressible Supercritical Fluids. *J. Phys. Chem. B* **2000**, *104*, 6248–6257.
- (54) Maddox, M. W.; Goodyear, G.; Tucker, S. C. Effect of Critical Slowing Down on Local-Density Dynamics. *J. Phys. Chem. B* **2000**, *104*, 6266–6270.
- (55) Berne, B. J.; Pecora, R. *Dynamic light scattering: with applications to chemistry, biology, and physics*; Courier Corporation, 2000.
- (56) Bondi, A. van der Waals Volumes and Radii. *J. Phys. Chem.* **1964**, *68*, 441–451.
- (57) Yardley, J. *Introduction to Molecular Energy Transfer*; Academic Press, New York, 1980.

Supporting Information: Energy Relaxation of N_2O in Gaseous, Supercritical and Liquid Xenon and SF_6

Kai Töpfer,[†] Shyamsunder Erramilli,[‡] Lawrence D. Ziegler,[¶] and Markus
Meuwly^{*,†,§}

[†]*Department of Chemistry, University of Basel, Klingelbergstrasse 80 , CH-4056 Basel,
Switzerland*

[‡]*Department of Physics and the Photonics Center, Boston University, 590 Commonwealth
Ave, MA 02215, Boston*

[¶]*Department of Chemistry and the Photonics Center, Boston University, 8 St Mary's St,
MA 02215, Boston*

[§]*Department of Chemistry, Brown University, Providence, RI 02912, USA*

E-mail: m.meuwly@unibas.ch

System Setup

Table S1: System setup of N₂O concentration $c(\text{N}_2\text{O})$, molar volumes V_m and critical density ratio ρ^* of one N₂O in 343 SF₆ molecules and one N₂O in 600 Xe atoms.

| N ₂ O/SF ₆ | | | N ₂ O/Xe | | |
|----------------------------------|---|----------|---------------------------------|---|----------|
| $c(\text{N}_2\text{O})$ (mol/l) | $V_m(\text{SF}_6)$ (cm ³ /mol) | ρ^* | $c(\text{N}_2\text{O})$ (mol/l) | $V_m(\text{Xe})$ (cm ³ /mol) | ρ^* |
| 0.20 | 4934 | 0.04 | 0.34 | 2984 | 0.04 |
| 0.51 | 1974 | 0.10 | 0.84 | 1194 | 0.10 |
| 0.81 | 1234 | 0.16 | 1.26 | 796 | 0.15 |
| 1.52 | 658 | 0.30 | 3.10 | 323 | 0.37 |
| 3.39 | 295 | 0.67 | 4.11 | 244 | 0.49 |
| 4.36 | 229 | 0.86 | 5.19 | 193 | 0.62 |
| 5.02 | 199 | 0.99 | 5.53 | 181 | 0.66 |
| 5.93 | 169 | 1.17 | 6.28 | 159 | 0.75 |
| 6.89 | 145 | 1.36 | 7.29 | 137 | 0.87 |
| 7.65 | 131 | 1.51 | 7.79 | 128 | 0.93 |
| | | | 11.14 | 90 | 1.33 |
| | | | 12.99 | 77 | 1.55 |

Table S2: Bonded and non-bonded parameters. Larger sets of parameters are made available on a github as full parameter files.

| Residues | Parameters | |
|---|---|------------------------------|
| N₂O | | |
| Intramolecular Potential RKHS ¹ | https://github.com/MMunibas/SCF_N2O/ in, e.g., N2O_Xe/source/pes1_rRz.csv or N2O_SF6/source/pes1_rRz.csv | |
| Electrostatic Potential polarizable MDCM ² | https://github.com/MMunibas/SCF_N2O/ in, e.g., N2O_Xe/source/n2o_xe.dcm or N2O_SF6/source/n2o_sf6.dcm | |
| Polarizabilities | α (1/Å ³) | |
| N1 | 0.94 | |
| N2 | 0.94 | |
| O | 0.94 | |
| Non-bonded in SF ₆ | ϵ_i (kcal/mol) | $R_{\min,i}/2$ (Å) |
| N1 | 0.2592 | 1.716 |
| N2 | 0.1542 | 1.618 |
| O | 0.2089 | 1.555 |
| Non-bonded in Xe | ϵ_i (kcal/mol) | $R_{\min,i}/2$ (Å) |
| N1 | 0.3775 | 1.637 |
| N2 | 0.0002 | 2.565 |
| O | 0.3684 | 1.497 |
| SF₆ | | |
| Samios and coworker ³ | | |
| Bonds | k_b (kcal/mol/Å ²) | r_{\min} (Å) |
| S-F | 165.746 | 1.565 |
| Angles | k_{Θ} (kcal/mol/rad ²) | Θ_{\min} (°) |
| F-S-F | 73.461 | 90.0 |
| Electrostatic Potential polarizable MDCM ² * | https://github.com/MMunibas/SCF_N2O/ in, e.g., N2O_Xe/source/n2o_xe.dcm or N2O_SF6/source/n2o_sf6.dcm | |
| Non-bonded | ϵ_i (kcal/mol) | $R_{\min,i}/2$ (Å) |
| S | 0.3257 | 1.822 |
| F | 0.0541 | 1.659 |
| Xe | | |
| Aziz and coworker ⁴ | | |
| Electrostatic Potential polarizable MDCM ² ** | q (e) | α (1/Å ³) |
| | 0.0 | 2.964 |
| Non-bonded Xe | ϵ_i (kcal/mol) | $R_{\min,i}/2$ (Å) |
| | 0.5610 | 2.181 |

* Contributing only to N₂O-SF₆ interaction

** Contributing effectively only to N₂O-Xe interaction

**Rotational energy autocorrelation function of N₂O
in Xe at 291.2 K**

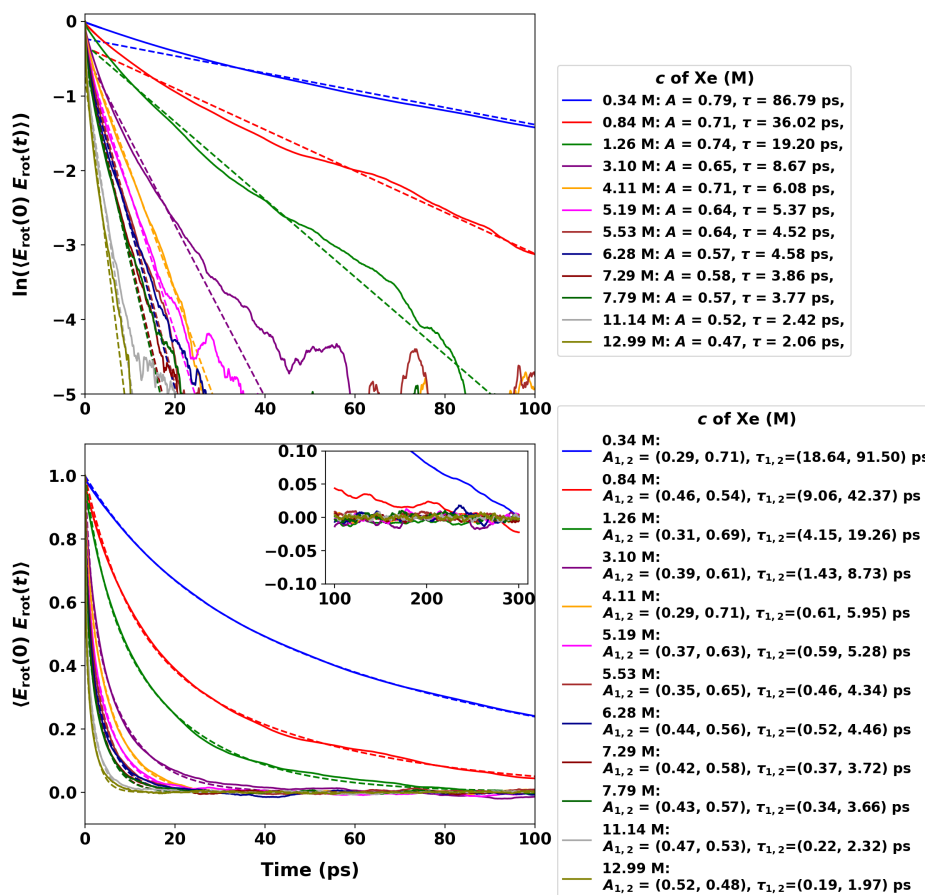


Figure S1: Rotational energy correlation function of N₂O in Xe at different solvent concentrations as solid lines and optimized fits of a the single-exponential function (top) to the logarithm and of a bi-exponential function (bottom) as dashed lines.

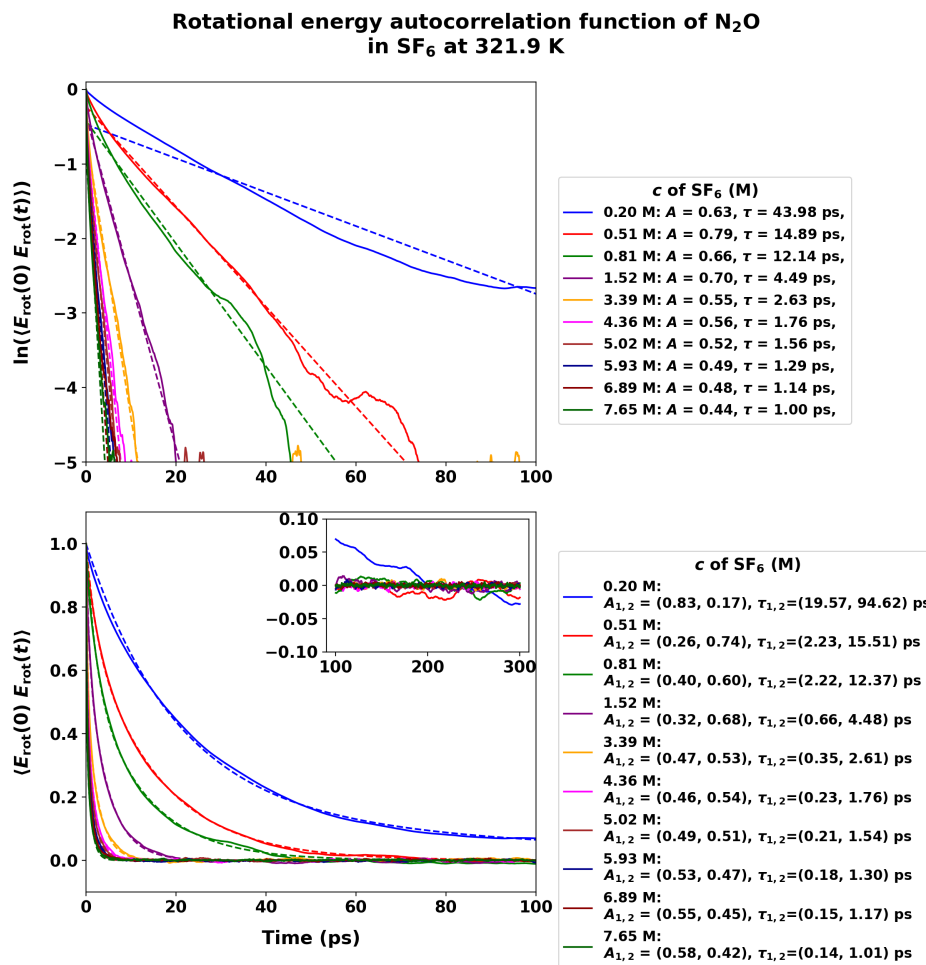


Figure S2: Rotational energy correlation function of N₂O in SF₆ at different solvent concentrations as solid lines and optimized fits of a the single-exponential function (top) to the logarithm and of a bi-exponential function (bottom) as dashed lines.

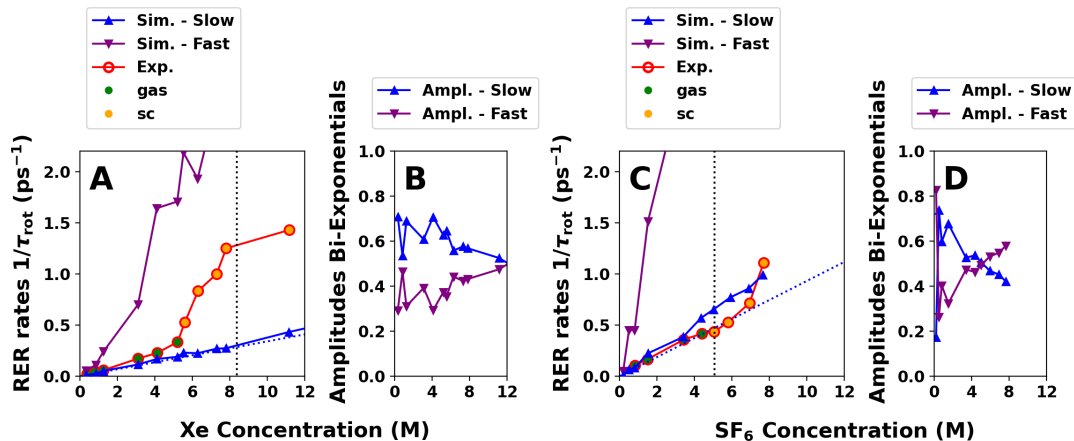


Figure S3: RER rates from the RER times $\tau_{rot,slow}$ and $\tau_{rot,fast}$ of a fitted bi-exponential function $C_2(t) = Ae^{-t/\tau_{fast}} + (1 - A)e^{-t/\tau_{slow}} + \Delta$ to correlation function of the rotational energy $E_{rot}(t)$ of N₂O in (A) xenon and (C) SF₆ at different solvent concentrations (solid blue lines). The solid red line with colored circle markers shows the experimentally measured RER rates and indicate the solvent state gaseous or supercritical (sc).⁵ The dotted blue line is an linear extrapolation of the first 3 simulated RER rates. The vertical dotted lines mark the experimentally observed solvent concentration at the respective critical density of xenon and SF₆, respectively. Panel B and D shows the amplitudes of the bi-exponential fit function for which the RER rates are shown in panel A and C, respectively.

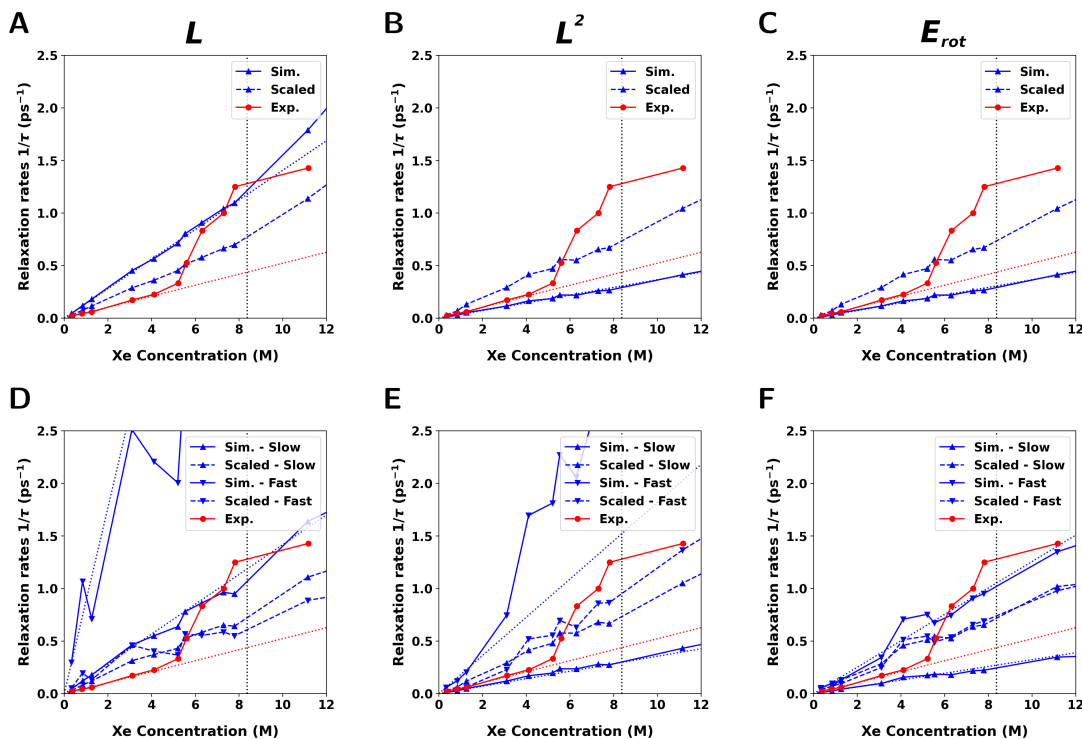


Figure S4: Rotational relaxation rates from the lifetimes of a fitted single- (A-C) and bi-exponential function (D-F) to correlation function of the angular momentum (A, D), squared angular momentum (B, E) or rotational energy (C, F) of N_2O in Xe and at different solvent concentrations. The solid red line with circle markers shows the experimentally measured rotational relaxation rates,⁵ and the dashed blue lines are the fitted rotational relaxation rates scaled to minimizing deviation from experiments. The vertical dashed lines mark the experimentally observed solvent concentration at the respective critical density xenon.

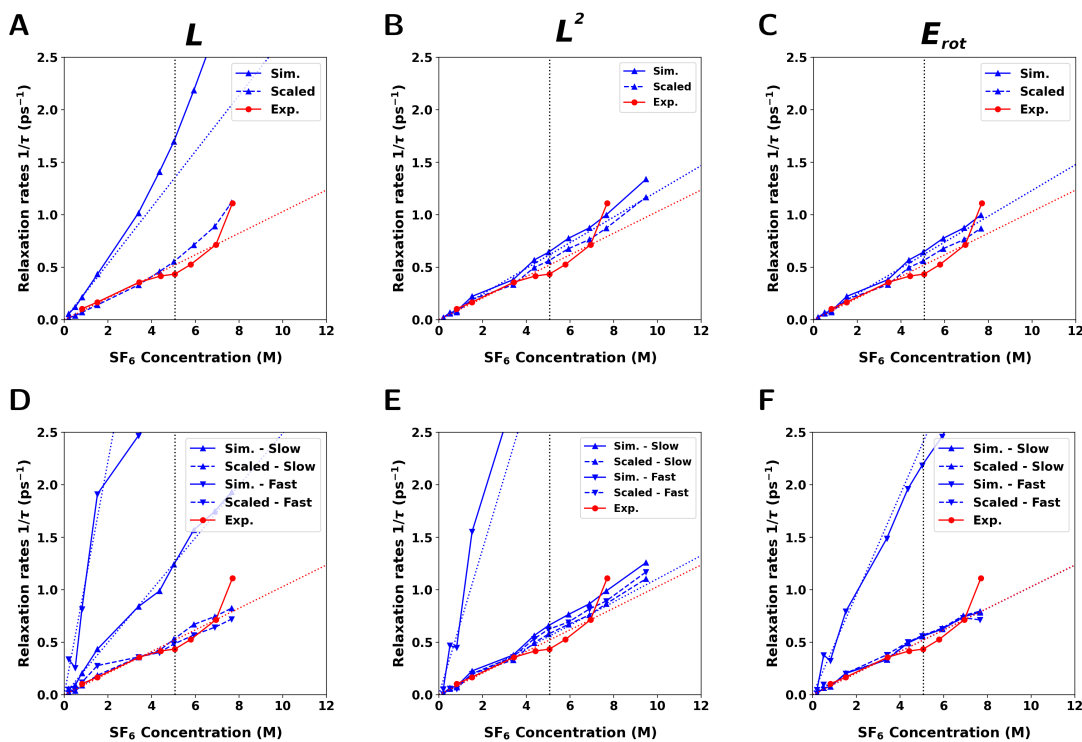


Figure S5: Rotational relaxation rates from the lifetimes of a fitted single- (A-C) and bi-exponential function (D-F) to correlation function of the angular momentum (A, D), squared angular momentum (B, E) or rotational energy (C, F) of N₂O in SF₆ and at different solvent concentrations. The solid red line with circle markers shows the experimentally measured rotational relaxation rates,⁵ and the dashed blue lines are the fitted rotational relaxation rates scaled to minimizing deviation from experiments. The vertical dashed lines mark the experimentally observed solvent concentration at the respective critical density SF₆.

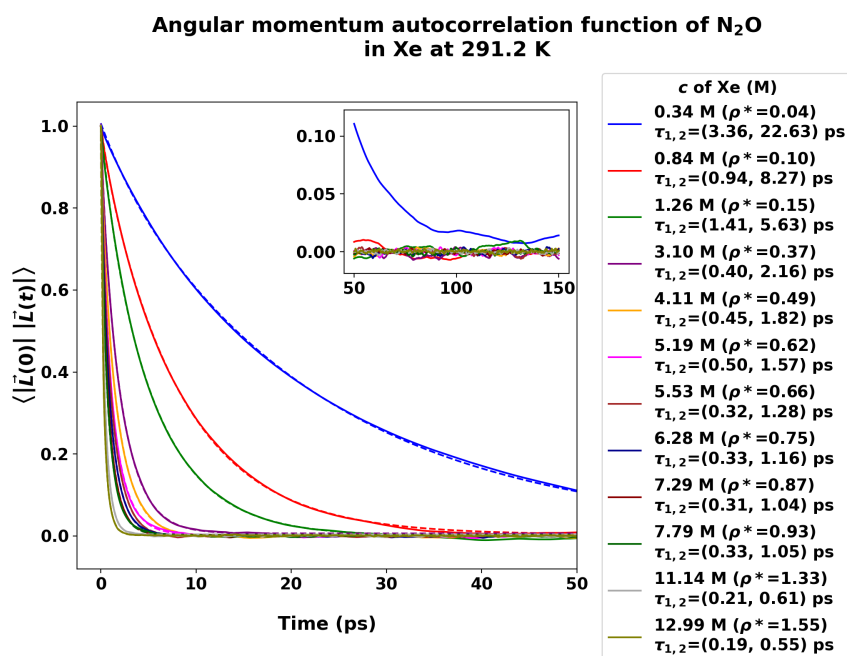
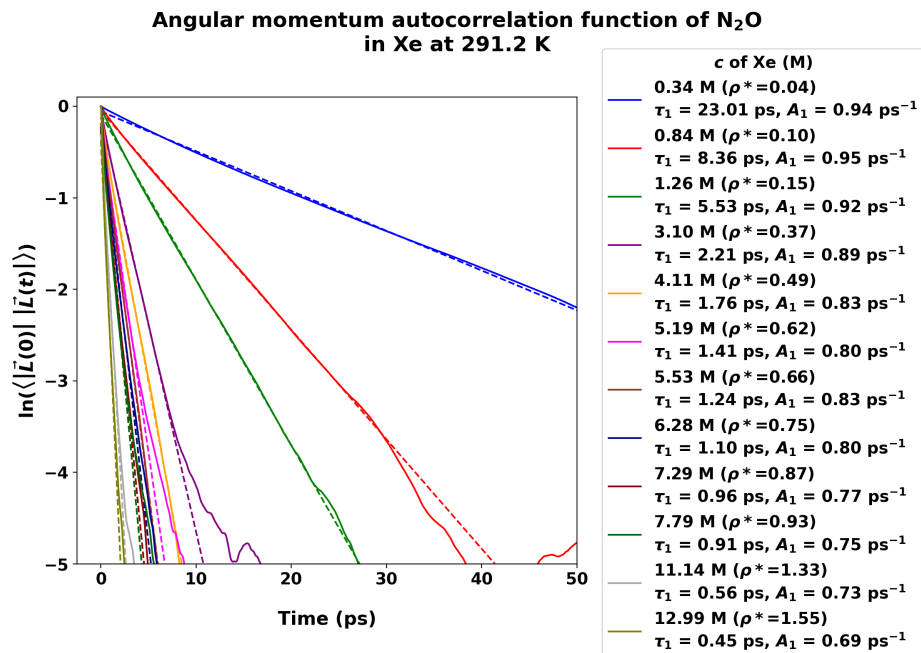


Figure S6: Angular momentum correlation function of N₂O in Xe at different solvent concentrations as solid lines and optimized fits of a the single-exponential function (top) to the logarithm and of a bi-exponential function (bottom) as dashed lines.

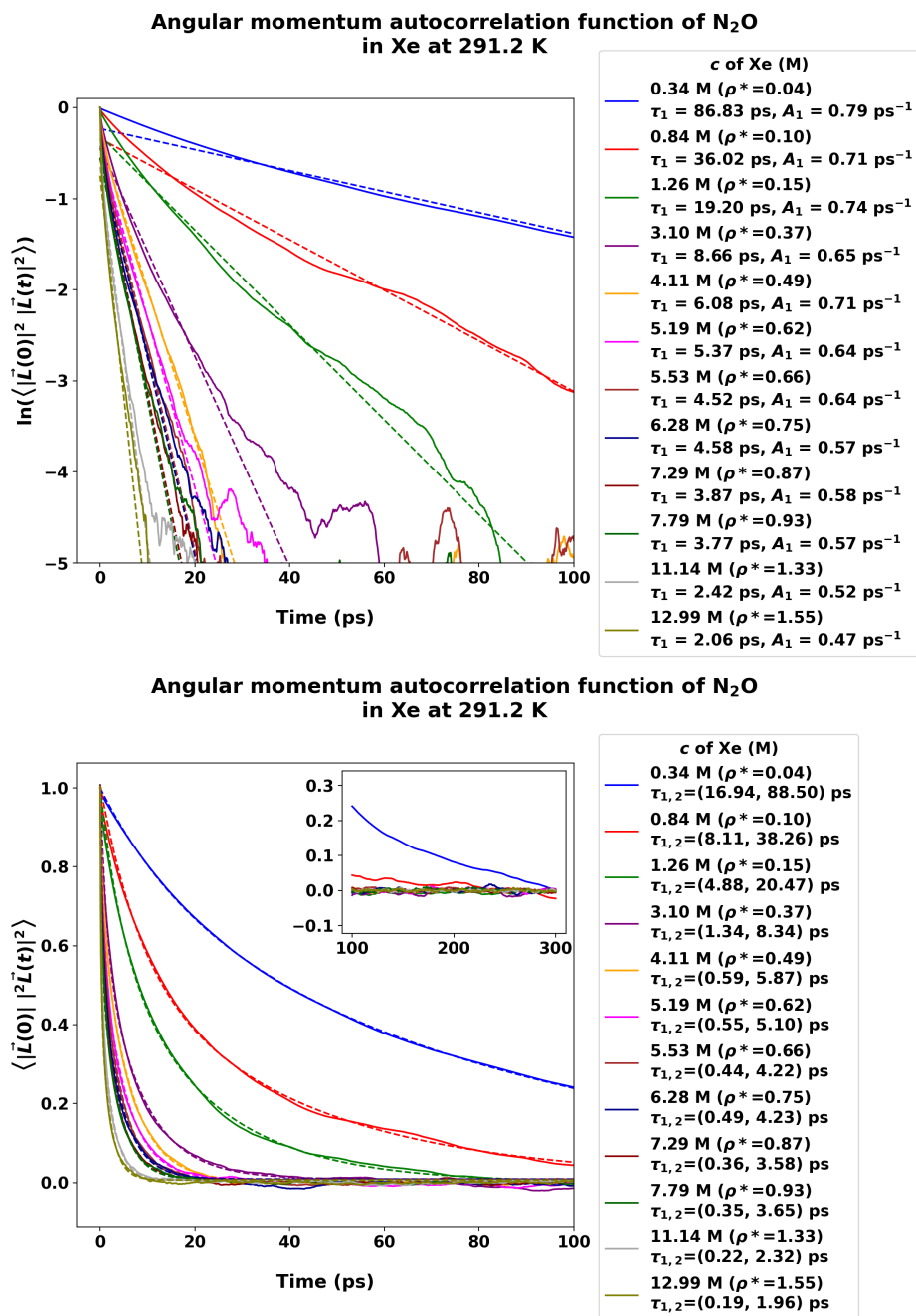
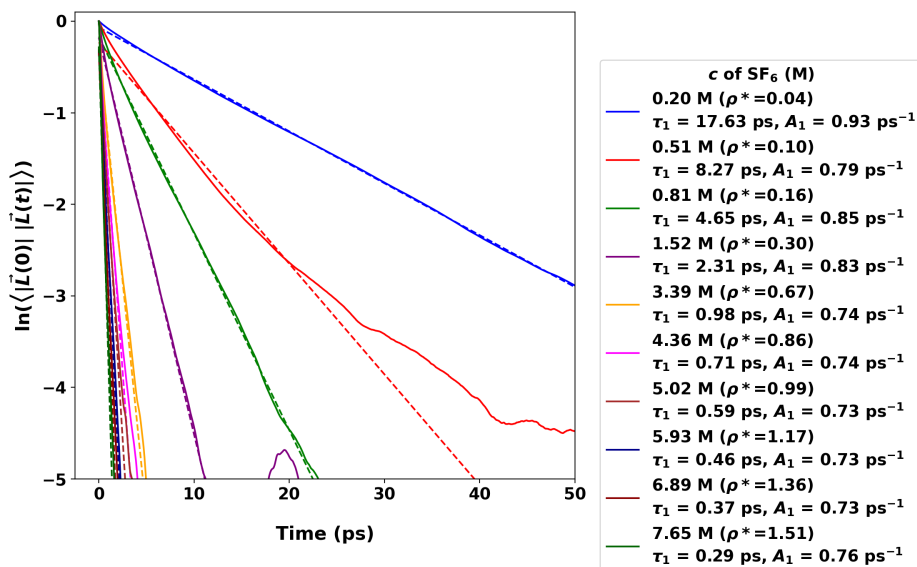


Figure S7: Squared angular momentum correlation function of N₂O in Xe at different solvent concentrations as solid lines and optimized fits of a the single-exponential function (top) to the logarithm and of a bi-exponential function (bottom) as dashed lines.

**Angular momentum autocorrelation function of N₂O
in SF₆ at 321.9 K**



**Angular momentum autocorrelation function of N₂O
in SF₆ at 321.9 K**

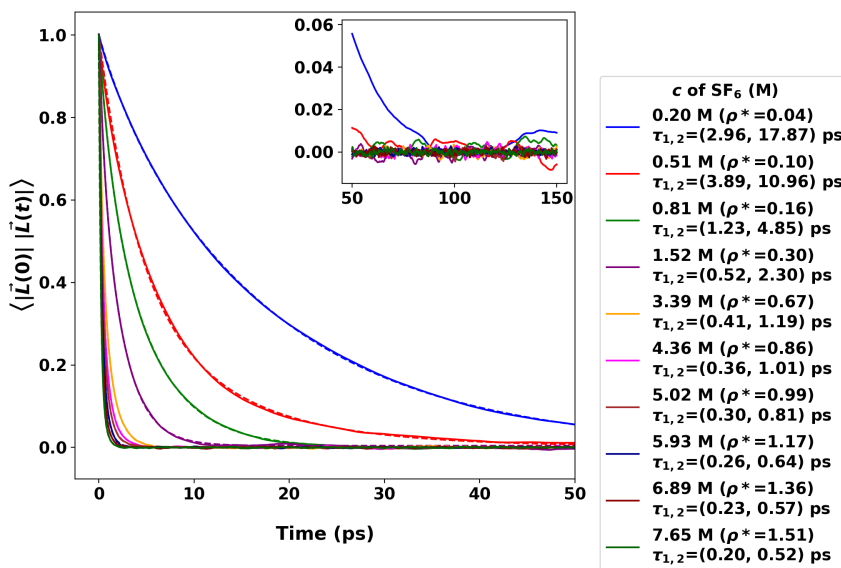
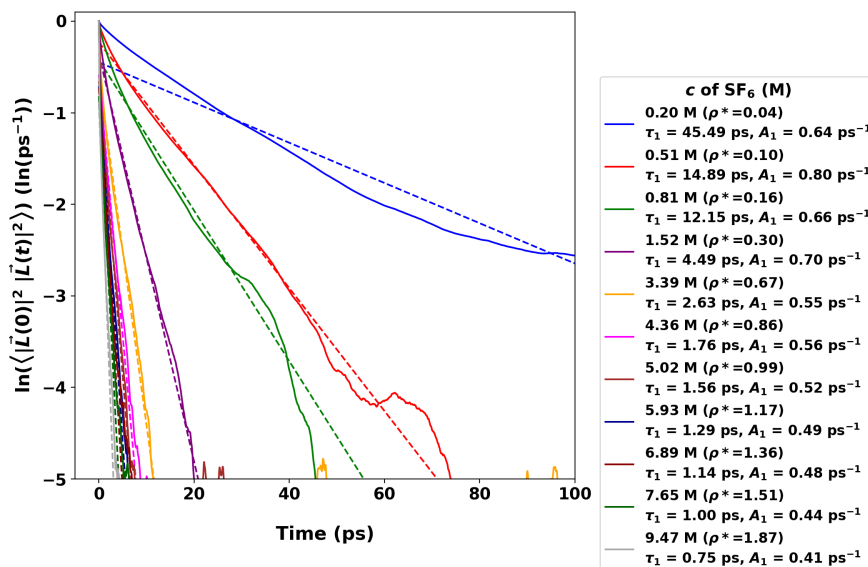


Figure S8: Angular momentum correlation function of N₂O in SF₆ at different solvent concentrations as solid lines and optimized fits of a the single-exponential function (top) to the logarithm and of a bi-exponential function (bottom) as dashed lines.

**Angular momentum autocorrelation function of N₂O
in SF₆ at 321.9 K**



**Angular momentum autocorrelation function of N₂O
in SF₆ at 321.9 K**

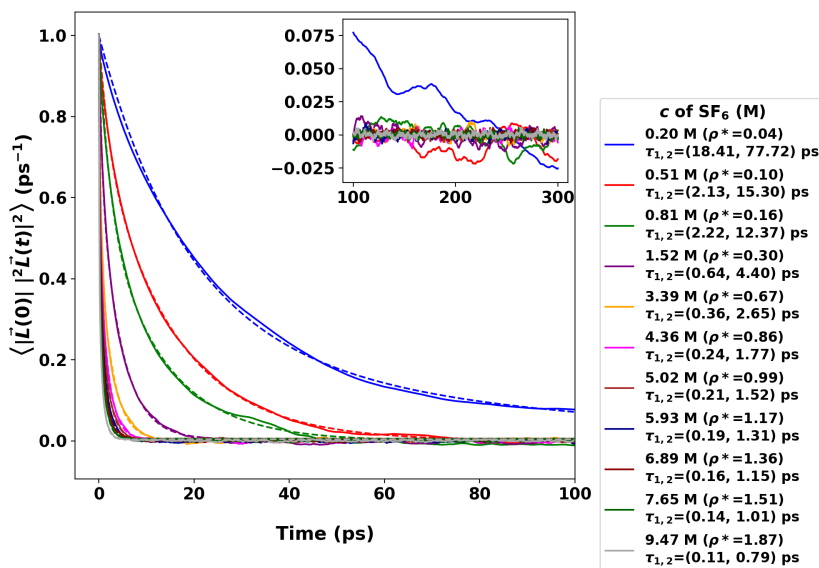


Figure S9: Squared angular momentum correlation function of N₂O in SF₆ at different solvent concentrations as solid lines and optimized fits of a the single-exponential function to the logarithm (top) and of a bi-exponential function (bottom) as dashed lines.

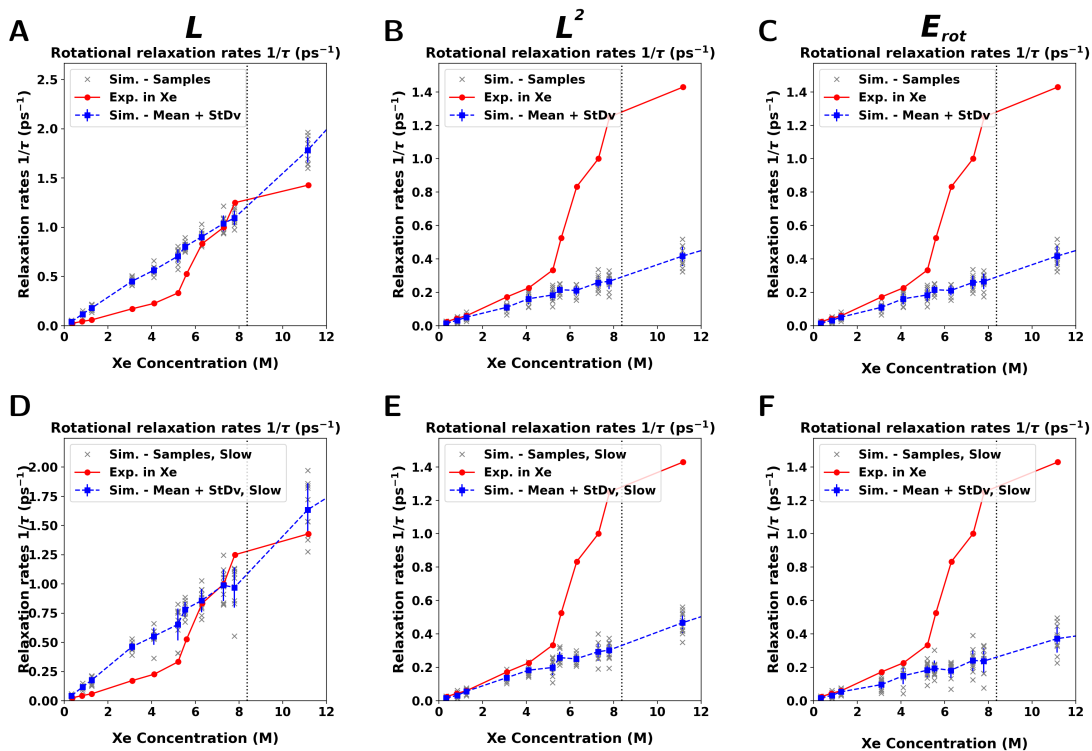


Figure S10: Rotational relaxation rates from the lifetimes of a fitted single- (A-C) and bi-exponential function (D-F) to correlation function of the angular momentum (A, D), squared angular momentum (B, E) or rotational energy (C, F) of N_2O in Xe and at different solvent concentrations. The solid red line with circle markers shows the experimentally measured rotational relaxation rates,⁵ and the dashed blue lines are the fitted rotational relaxation rates scaled to minimizing deviation from experiments. The vertical dashed lines mark the experimentally observed solvent concentration at the respective critical density xenon.

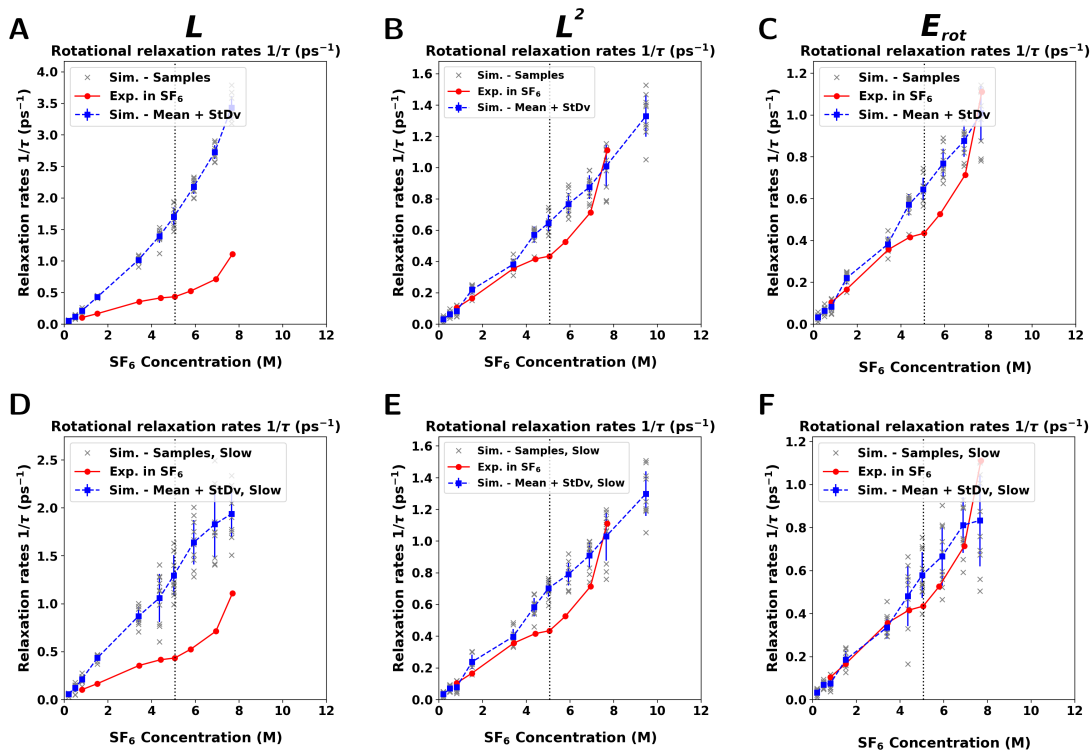


Figure S11: Average of obtained rotational relaxation rates from the lifetimes of a fitted single- (A-C) and bi-exponential function (D-F) to the single correlation functions of the angular momentum (A, D), squared angular momentum (B, E) or rotational energy (C, F) of each sample run of N_2O in SF_6 and at different solvent concentrations (solid blue line). The grey markers . The solid red line with circle markers shows the experimentally measured rotational relaxation rates,⁵ and the dashed blue lines are the fitted rotational relaxation rates scaled to minimizing deviation from experiments.

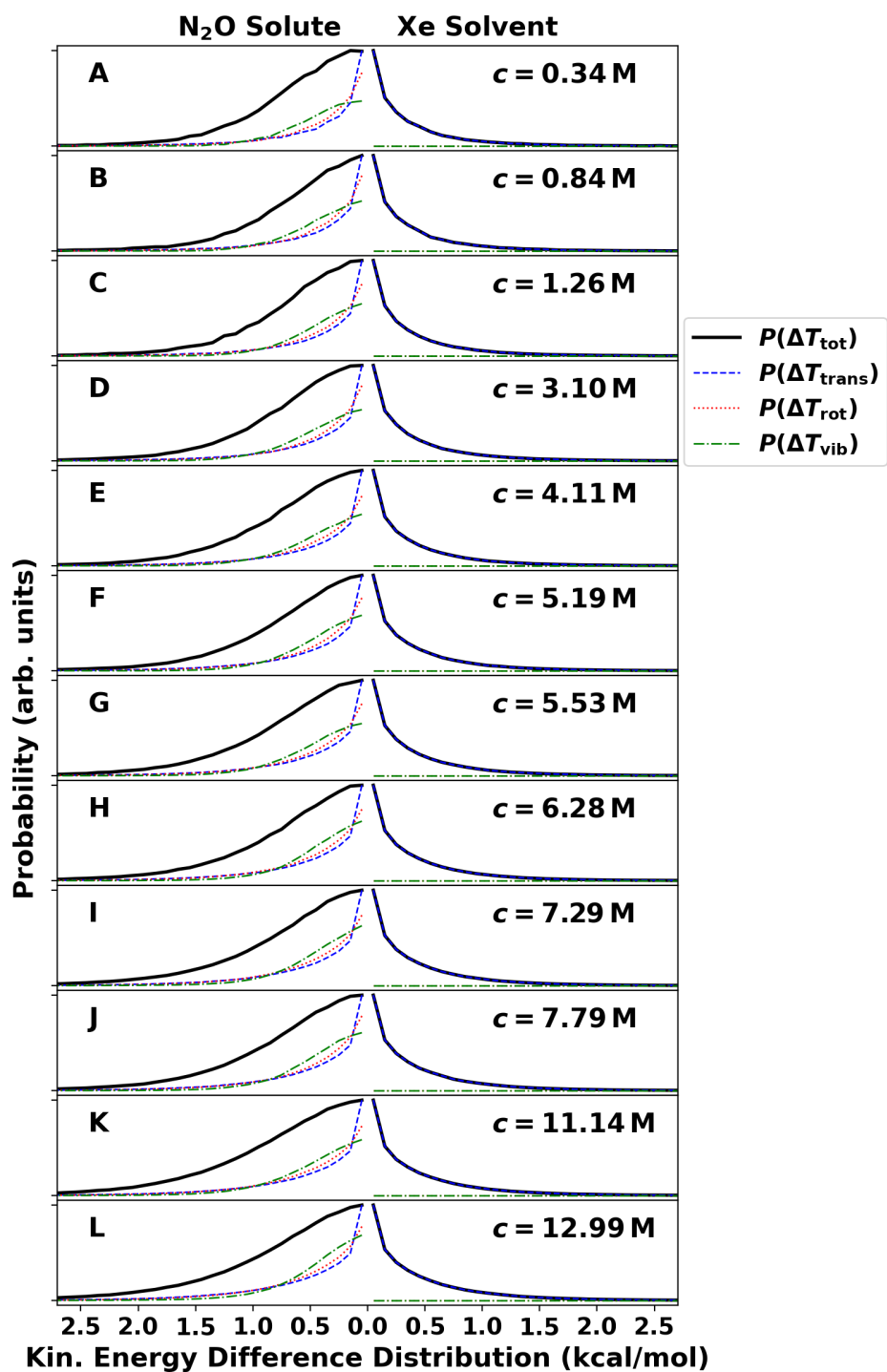


Figure S12: Absolute Kinetic energy difference probability distribution $P(\Delta T)$ of the total, translational, rotational and vibrational kinetic energy in N_2O after an collision event with a xenon solvent atom for different solvent concentrations. Left part of the axis shows the $P(\Delta \bar{T})$ for the N_2O solute and right part for the xenon solvent.

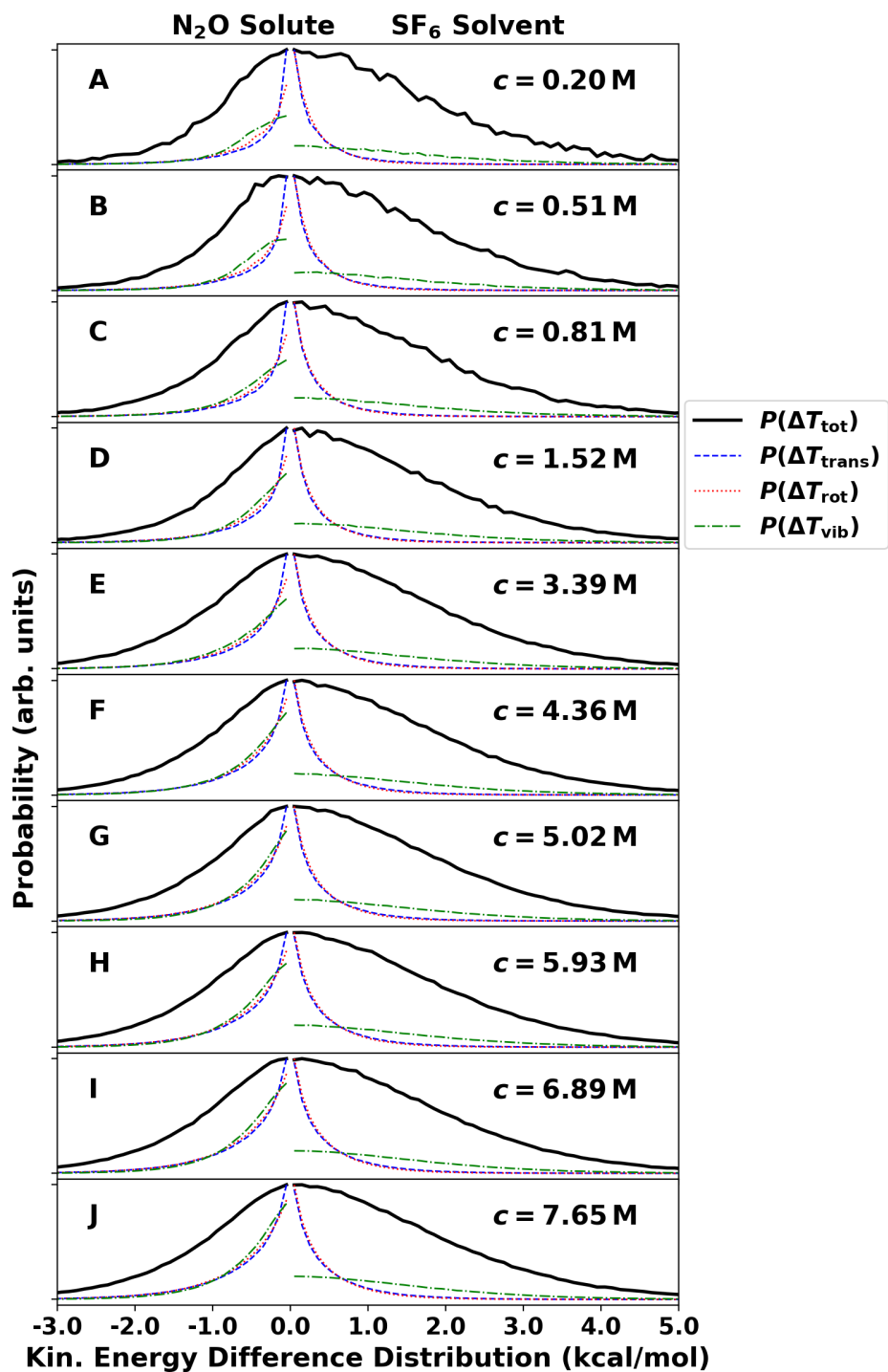


Figure S13: Absolute Kinetic energy difference probability distribution $P(\Delta T)$ of the total, translational, rotational and vibrational kinetic energy in N_2O after a collision event with a SF_6 solvent molecule for different solvent concentrations. Left part of the axis shows the $P(\Delta \bar{T})$ for the N_2O solute and right part for the SF_6 solvent.

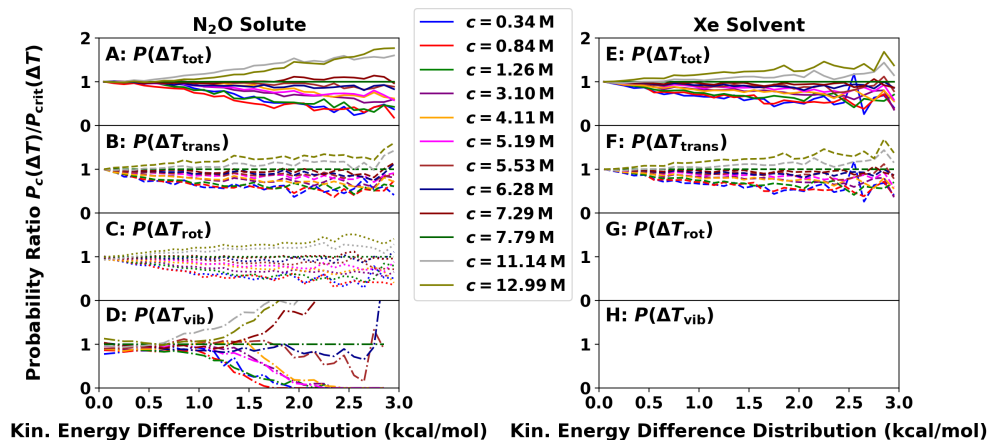


Figure S14: Kinetic energy difference probability distribution ratio $P_c(\Delta T)/P_{\text{crit}}(\Delta T)$ between the absolute kinetic energy difference probability distribution $P_c(\Delta T)$ at solvent concentration c and the respective distribution closest to the critical distribution $P_{\text{crit}}(\Delta T)$ at $c_{\text{crit}} \approx 7.79$ M.

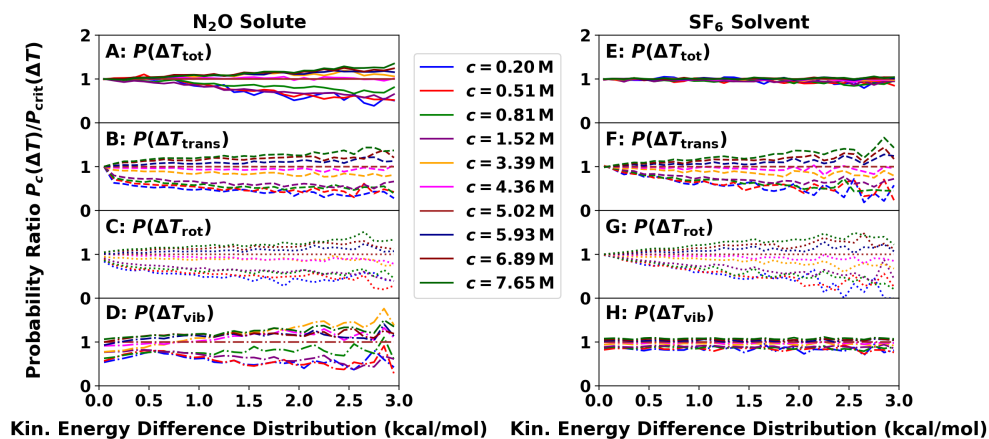


Figure S15: Kinetic energy difference probability distribution ratio $P_c(\Delta T)/P_{\text{crit}}(\Delta T)$ between the absolute kinetic energy difference probability distribution $P_c(\Delta T)$ at solvent concentration c and the respective distribution at the critical distribution $P_{\text{crit}}(\Delta T)$ at $c_{\text{crit}} \approx 5.02$ M.

**Logarithm of the Fourier transformed N₂O force along mode 9
in Xe at 291.2 K**

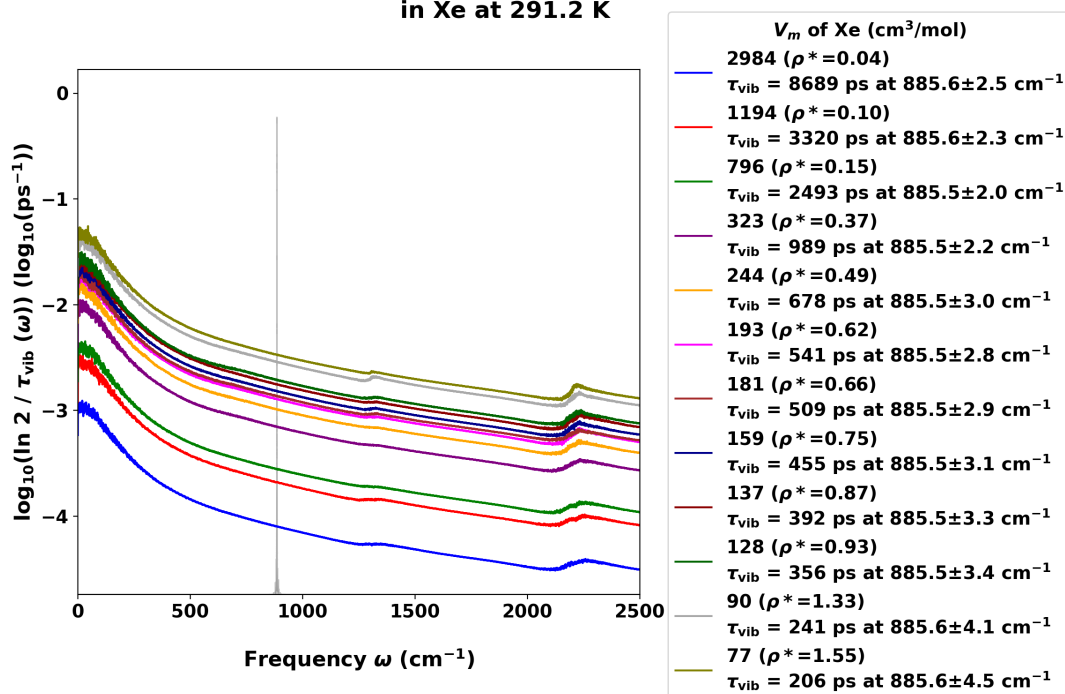


Figure S16: Frequency dependent friction function for the vibrational transition $\nu_s, \nu_{\text{as}} = 0, 1$ to $\nu_s, \nu_{\text{as}} = 1, 0$ of N₂O in xenon at different solvent concentration. The gray histogram shows the average transition frequency for all solvents and the transition frequency mean and standard deviation is given in the legend with the respective vibrational relaxation value τ_{vib} .

**Logarithm of the Fourier transformed N₂O force along mode 9
in SF₆ at 321.9 K**

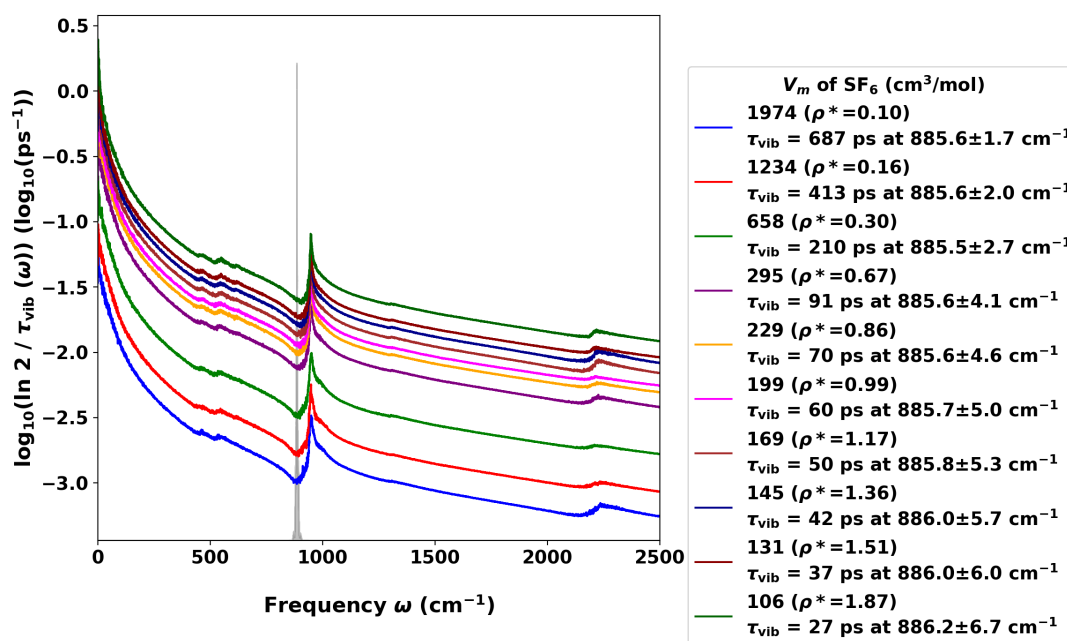


Figure S17: Frequency dependent friction function for the vibrational transition $\nu_s, \nu_{\text{as}} = 0, 1$ to $\nu_s, \nu_{\text{as}} = 1, 0$ of N₂O in SF₆ at different solvent concentration. The gray histogram shows the average transition frequency for all solvents and the transition frequency mean and standard deviation is given in the legend with the respective vibrational relaxation value τ_{vib} . The vertically dotted magenta line show the position of the SF₆ stretch frequency at 762 cm^{-1} . The dashed green line next to it is shifted by -8 cm^{-1} which is the experimentally measured frequency difference between the SF₆ stretch and the transition frequency between the N₂O stretch vibrations.

References

- (1) Koner, D.; San Vicente Veliz, J. C.; Bemish, R. J.; Meuwly, M. Accurate reproducing kernel-based potential energy surfaces for the triplet ground states of N₂O and dynamics for the N + NO \leftrightarrow O + N₂ and N₂ + O \rightarrow 2N + O reactions. *Phys. Chem. Chem. Phys.* **2020**, *22*, 18488–18498.
- (2) Devereux, M.; Pezzella, M.; Raghunathan, S.; Meuwly, M. Polarizable Multipolar Molecular Dynamics Using Distributed Point Charges. *J. Chem. Theo. Comp.* **2020**, *16*, 7267–7280.
- (3) Dellis, D.; Samios, J. Molecular force field investigation for Sulfur Hexafluoride: A computer simulation study. *Fluid Phase Equilib.* **2010**, *291*, 81–89.
- (4) Aziz, R. A.; Slaman, M. On the Xe-Xe potential energy curve and related properties. *Mol. Phys.* **1986**, *57*, 825–840.
- (5) Rotondaro, M. C.; Jain, A.; Erramilli, S.; Ziegler, L. D. Ultrafast 2DIR comparison of rotational energy transfer, isolated binary collision breakdown, and near critical fluctuations in Xe and SF₆ solutions. *J. Chem. Phys.* **2022**, *157*, 174305.